# Nitrogen-carbon-encapsulated Fe₃C nanoparticles as highly efficient earth-abundant oxygen reduction electrocatalysts

Cuiping Wang [1], Zhi Li [1*], Jie Lei [1], Song Li [1], Stijn F. L. Mertens [2*], Jinsong Hu [1, 3*]

ABSTRACT The design and synthesis of highly active MOF-based catalysts opens new avenues to facilitate the kinetically unfavorable oxygen reduction reaction (ORR) process. Here, we shed light on the design and fabrication of an efficient electrocatalyst with novel structure for the enhancement of ORR performance, by decorating the surface of ZIF-8 precursor with ferrocene formic acid, followed by a two-step carbonization process, which is critical for the encapsulation of pyrolytic Fe₃C nanoparticles into carbon nanotubes (CNTs) and the isolation of Fe single atoms onto N-doped carbon (NC) matrix. In addition, the relative content of Fe element is vital to optimize the ORR performance of the catalysts. The resulting Fe₃C@CNTs/NC-M catalyst has an advanced structure and shows great long-term stability and excellent electrocatalytic ORR performance in alkaline solution, with the half-wave potential and limiting current reaching 0.941 V and 6.31 mA/cm², respectively. Furthermore, the electrocatalyst has a strong tolerance against and good stability in methanol solution. Fe₃C@CNTs/NC-M zinc-air battery (ZAB) exhibits a large 1.525 V open-circuit potential, a 348 mW/cm² peak power density at 420 mA/cm², and a 843 mAh/g·$_{Zn}^{-1}$ maximum capacity at 10 mA/cm². Therefore, this synthetic strategy provides a promising pathway towards constructing MOF based electrocatalytic materials with effective and stable ORR performance.

Keywords: Metal-organic frameworks, CNTs, N-doped carbon matrix, Oxygen reduction reaction, Zn-air battery

## INTRODUCTION

As the depletion of fossil fuels has become significant with the rapid advancement of industrialization [1], non-renewable energy reserves are facing severe shortages [2,3] and major environmental issues are increasingly apparent. In response to these urgencies, mineral fuels must be substituted by green and renewable energy sources [4,5]. This ongoing energy transition is accompanied by a rapid increase in the use of metal-air batteries [6] and fuel cells [7,8], in which the oxygen reduction reaction (ORR) plays a central role. Poor kinetics of the ORR is responsible for considerable energy losses, so that the development of ORR catalysts that make the oxygen reduction overpotential as small as possible has emerged as a critical research focus [9].

With this goal, rare and expensive noble metals have been widely employed as ORR electrocatalysts due to their excellent catalytic performance in alkaline media, but their cost and low abundance prohibit their widespread use. Therefore, a strong focus exists to replace rare metals with highly efficient, earth-abundant and non-precious ORR electrocatalysts. Among these, transition metal organic frameworks (MOFs) show considerable promise for catalytic energy conversion and storage [10], as their large specific surface area [11], porosity [12], adjustability [13], and abundant unsaturated coordination sites [14] give access to a vast variety of electrocatalysts. Pyrolysis of MOF precursors has been explored as a practical method to generate transition metal-based nitrogen-doped carbon matrix (M-NC) [15-17] for promoting electrocatalytic processes [18,19], and retains high porosity, large electroactive area and abundant unsaturated coordination sites, while providing adjustable nitrogen doping, and high conductance from a high degree of graphitization. In particular, zeolite imidazole frameworks (ZIFs) with high nitrogen content and pore volume were shown to be suitable precursors for nanostructured N-doped carbon composites through diverse pyrolysis pathways [20,21].

In previous work, catalytic materials such as metal carbides, metal sulfides, and metal oxides nanoparticles (NPs) were obtained by heat treatment of MOF precursors, resulting in active metals embedded in a carbon matrix for catalyzing ORR [22,23]. Recently, Fe₃C NPs were shown to boost ORR in multi-metal M-NC based catalysts [24-26], but many questions remain, including the possibility of synergistic effects and the impact of Fe₃C NP size and concentration on the ORR performance [27,28]. Therefore, it is meaningful to systematically investigate the function of Fe₃C NPs in M-NC based electrocatalysts without the interference of other metal elements in ORR. The synergistic effect of carbon nanotubes (CNTs) and porous carbon matrices

[1] School of Chemical Engineering, Anhui Province Key Laboratory of Specialty Polymers, Anhui University of Science and Technology, Huainan 232001, China
[2] Department of Chemistry, Energy Lancaster and Materials Science Lancaster, Lancaster University, Lancaster LA1 4YB, United Kingdom
[3] Institute of Energy, Hefei Comprehensive National Science Center, Anhui, Hefei 230031, China
* Corresponding authors (email: 2022025@aust.edu.cn (Z. Li); s.mertens@lancaster.ac.uk, stmerten@gmail.com (S. F. L. Mertens); jshu@aust.edu.cn (J. Hu))

in providing larger contact area [29], more catalytic sites, and improving the interfacial contact between electrolyte and catalyst is well known [30,31]. Importantly, CNTs improve electronic conduction and limit resistive losses [32], and also slow down the deactivation of catalytic sites[33], prolonging the lifetime of catalysts during ORR [34,35]. Although many NP/CNT composites have been explored for electrocatalysis, $Fe_3C$/CNT materials have been less studied due to lack of effective preparation methods.

In this work, we demonstrate a facile synthetic strategy that uses a metal-containing ligand (ferrocenecarboxylic acid, FcCOOH) to decorate the surface of ZIF-8, followed by a two-step carbonization process for preparing $Fe_3C$@CNTs/NC-x catalysts. The first carbonization step is conducted at 920 °C to reduce the interference of Zn from the sacrificial ZIF-8 template and form $Fe_3C$ nanoparticles, while the second step promotes template reconstruction and the conversion of C and N to a CNT decorated NC conducting framework. Growing $Fe_3C$ nanoparticles in a matrix of CNTs and NC conducting framework may promote the electrochemical stability of electrocatalysts and enhance their ORR electrocatalytic performance, similar as recently demonstrated for covalently bound $Bi_2S_3$/graphene composites [36]. We also systematically analyze the impact of the Fe content in the $Fe_3C$@CNTs/NC-x on ORR electroactivity. The optimized $Fe_3C$@CNTs/NC-M achieves ORR electrocatalytic activity characterized by $E_{1/2}$=0.941 V vs RHE and $J_k$=6.31 mA/cm$^2$ in 0.1 M KOH solution. Furthermore, a primary zinc-air battery assembled using $Fe_3C$@CNTs/NC-M as the air cathode yields an open circuit voltage (OCV) of 1.525 V and a power density up to 348 mW/cm$^2$ at 420 mA/cm$^2$, exceeding most carbon-based electrocatalysts reported to date under similar conditions. These encouraging results will promote the application of the $Fe_3C$@CNTs/NC catalysts for ORR and beyond.

## EXPERIMENTAL SECTION

Synthesis of ZIF-8: 396.7 mg zinc nitrate hexahydrate and 410.6 mg 2-methylimidazole (2-meim) were dissolved in 20 mL anhydrous methanol, followed by continuous stirring for 30 min. The solid ZIF-8 was collected after centrifugation and washing with N,N-dimethylformamide (DMF) and anhydrous methanol twice, followed by vacuum drying at 50 °C overnight.
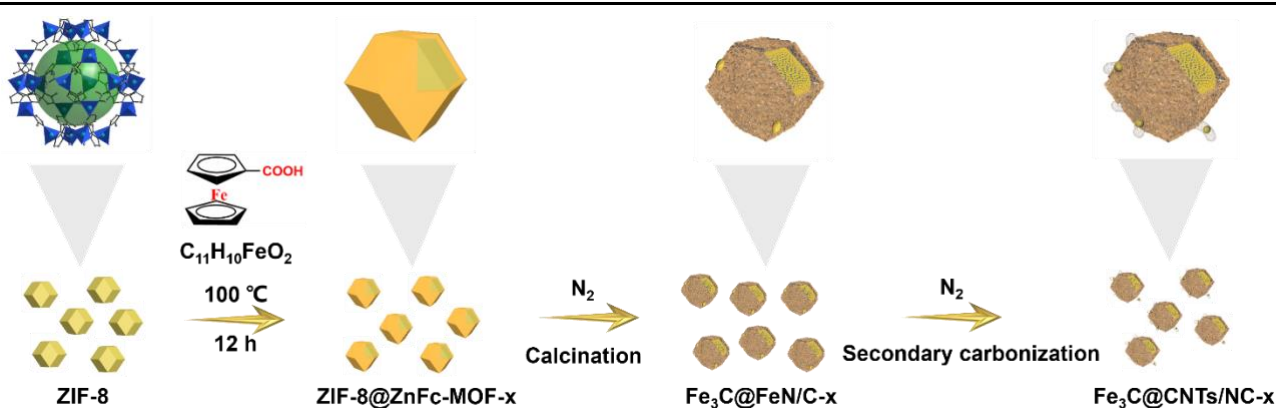
Synthesis of ZIF-8@ZnFc-MOF-x: ZIF-8@ZnFc-MOF-x was synthesized following a two-step approach. Taking the synthesis procedure of ZIF-8@ZnFc-MOF-M as an example, 2 mL ZIF-8 (10 mg/mL) suspension in methanol was mixed with 2 mL FcCOOH (2.5 mg/mL) DMF solution and placed in a polytetrafluoroethylene-lined steel vessel for hydrothermal synthesis. After 12 h hydrothermal treatment at 100 °C , the precipitate was obtained after centrifugation at 8000 rpm, washed 3 times with methanol and dried in a vacuum oven overnight at 50 °C . The ZIF-8@ZnFc-MOF-x precursors were synthesized by combining 2, 5 and 10 mg FcCOOH with 20 mg ZIF-8, and are denoted as ZIF-8@ZnFc-MOF-L, ZIF-8@ZnFc-MOF-M, ZIF-8@ZnFc-MOF-H, respectively. ZIF-8/FcCOOH-Mix was prepared by mechanical grinding of 20 mg ZIF-8 and 5 mg FcCOOH using an agate mortar and pestle.

Synthesis of Fe $Fe_3C$@CNTs/NC-x: The ZIF-8@ZnFc-MOF-x precursor underwent carbonization by heating to 920 °C under nitrogen flow using a 5 °C /min heating rate and maintaining the temperature for 2 h, followed by natural cooling to room temperature. Black precipitates were obtained after 24 h treatment in 0.5 M $H_2SO_4$ acid, centrifugation at 8000 rpm, washing twice with deionized water, and vacuum drying at 50 °C overnight. The prepared samples are denoted as $Fe_3C$@FeN/C-x. A second carbonization process, following the same procedure as the first, resulted in yellow powders denoted as $Fe_3C$@CNTs/NC-x. The catalysts prepared by pure ZIF-8, ZIF-8@ZnFc-MOF-L, ZIF-8@ZnFc-MOF-M, ZIF-8@ZnFc-MOF-H and ZIF-8/FcCOOH-Mix are named NC, $Fe_3C$@CNTs/NC-L, $Fe_3C$@CNTs/NC-M, $Fe_3C$@CNTS/NC-H and $Fe_3C$@CNTs/NC-Mix, respectively.

## RESULTS

Scheme 1 outlines the overall synthesis of $Fe_3C$@CNTs/NC-x catalysts. The ZIF-8 precursor undergoes solvothermal treatment in the presence of FcCOOH ligand to form ZIF-8@ZnFc-MOF-x, followed by a two-step carbonization process to form the final $Fe_3C$@CNTs/NC-x catalyst. The first carbonization step reduces the metal interference of Zn from the sacrificial ZIF-8 template and forms $Fe_3C$ NPs. The second carbonization step is critical for boosting the ORR performance of $Fe_3C$@CNTs/NC-x. In the second stage of carbonization, carbon nanotubes are formed through the catalytic action of Fe.  At sufficiently high temperature, carbon-containing precursors decompose, and the limited solubility of carbon in transition metals causes CNTs to nucleate and grow on top of the catalyst [33]. Fig. S1 shows that the ORR performance of $Fe_3C$@CNTs/NC-M ($E_{1/2}$ = 0.941 V; $J_k$ = 6.31 mA/cm$^2$) formed in secondary carbonization process is greater than that of $Fe_3C$@FeN/C-M ($E_{1/2}$ = 0.921 V; $J_k$ = 6.15 mA/cm$^2$) formed during the primary carbonization process, due to the formation of CNTs for the encapsulation of $Fe_3C$ NPs and the reconstruction of the NC framework.

Scheme 1. The synthesis procedure of Fe₃C@CNTs/NC-x

The morphologies of ZIF-8, ZIF-8@ZnFc-MOF-M, and Fe₃C@CNTs/NC-M were probed by scanning electron microscopy (SEM). A clear dodecahedral structure for both ZIF-8 and ZIF-8@ZnFc-MOF-M is visible in Figs. 1a-1b and S2-S5. The addition of FcCOOH did not change the original morphology and size (around 1 μm) of the ZIF-8 template. The uniform distribution of C, N, O, Zn, and Fe in the ZIF-8@ZnFc-MOF-M EDS elemental mapping, Fig. S6, is a clear indication that FcCOOH is successfully attached to the surface of ZIF-8. The change in color between ZIF-8 (white) and ZIF-8@ZnFc-MOF-M (pale yellow), Fig. S7, is a further indication of a chemical transformation, rather than simple mixing, on attachment of FcCOOH to ZIF-8. To better understand the details of the high-temperature annealing step in N₂ atmosphere, the carbonization process was probed by thermogravimetry, Fig. S8. The mass change below 200 ℃ is ascribed to the loss of solvent molecules outside and inside the cavities and channels of the structure. Between 200 and 800 ℃, there is a gradual mass loss due to the carbonization of ligands. In addition, at these temperatures, the formed elemental carbon can reduce part of the $Zn^{2+}$ to form metallic Zn which can subsequently evaporate. At much higher temperatures, however, excessive sintering may again reduce the performance of the catalysts. Fig. S9 shows that the catalytic ORR performance of catalysts generated at 800 ℃ is poor ($E_{1/2}$ = 0.886 V; $J_k$ = 6.11 mA/cm²) and at 1000 °C is also compromised ($E_{1/2}$ = 0.9137 V; $J_k$ = 5.58 mA/cm²), compared to that at 920 ℃. Therefore, 920 ℃ is identified as optimal carbonization temperature. Furthermore, the first carbonization process causes a moderate sintering of the ZIF-8@ZnFc-MOF-M template with the preservation of the dodecahedral morphology but the enlargement of the grain size from 1 to around 2 μm, Fig. S10.

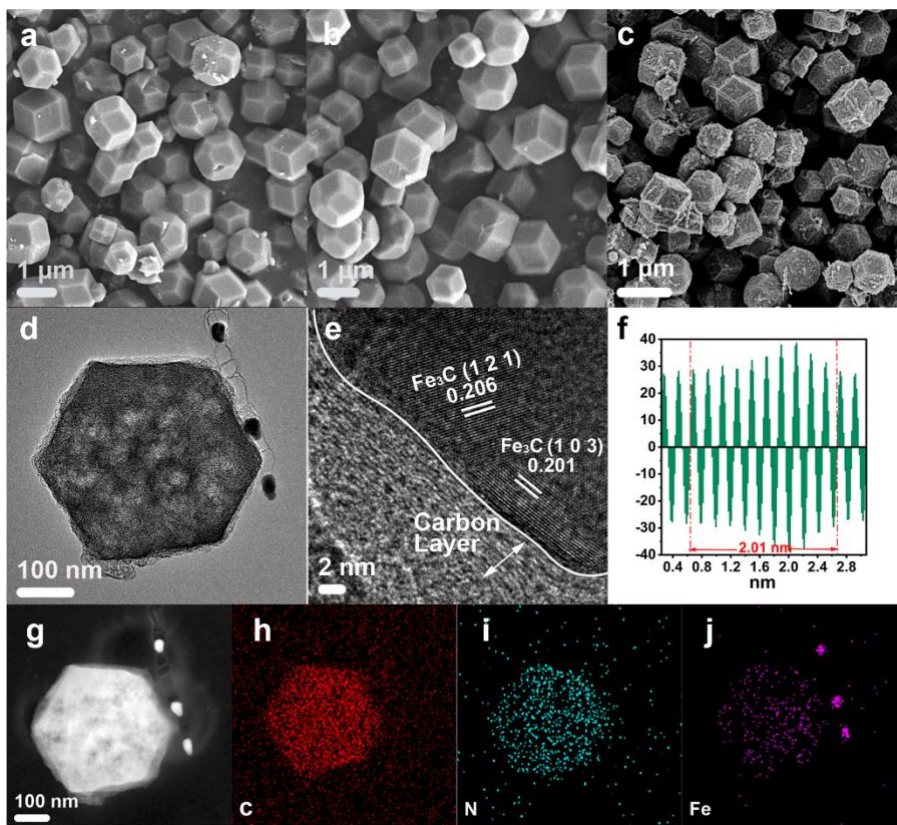Figure 1 SEM images of (a) ZIF-8; (b) ZIF-8@ZnFc-MOF-M, and (c) $Fe_3C@CNTs/NC-M$; (d) Bright field TEM image of $Fe_3C@CNTs/NC-M$; (e)-(f) Lattice analysis of $Fe_3C@CNTs/NC-M$; (g) Dark field STEM image of $Fe_3C@CNTs/NC-M$; (h)-(j) EDS mappings of $Fe_3C@CNTs/NC-M$

After the second carbonization, $Fe_3C@CNTs/NC-x$ catalysts were formed with three different Fe concentrations, which were determined by inductively coupled plasma–optical emission spectrometry (ICP-OES) as 0.25, 1.46 and 2.19 mass% in $Fe_3C@CNTs/NC-L$, $Fe_3C@CNTs/NC-M$, $Fe_3C@CNTs/NC-H$, respectively. The microstructure of the $Fe_3C@CNTs/NC-x$ catalysts and all the control samples was analyzed by scanning electron microscopy (SEM, Fig. 1c and S11-S15) and transmission electron microscopy (TEM, Fig. 1d). The original dodecahedral structure was maintained for all the samples, but the surface became rougher and the cluster size decreased to approximately 500 nm, due to the shrinkage of the original template and the reconstruction of the NC framework upon the secondary 920 ℃ annealing. The formation of CNTs was clearly observed on the dodecahedral framework in the TEM image after the secondary carbonization process, Fig. 1d and S16. The lattice fringes inside the nanoparticles correspond to the (1 0 3) and (1 2 1)

planes of $Fe_3C$, Fig. 1e and 1f, with representative lattice spacings of 0.201 and 0.206 nm. $Fe_3C$ nanoparticles can regulate the electronic structure of $Fe-N_x$ site, which can not only improve the interfacial conductivity, but also facilitate the electron transfer during ORR catalysis [27,37]. CNTs provide a larger contact area, more catalytic sites, and improved interface contact between the electrolyte and catalyst. Importantly, CNTs improve electron conduction, limiting resistive losses, and also slow down the deactivation behavior of catalytic sites, extending the lifetime of the catalyst during ORR [38]. Encapsulation with $Fe_3C$ can alter the electronic structure of CNTs, consequently improving the intrinsic activity of oxygen-containing functional groups on the surface of CNTs and increasing the degree of graphitization for rapid electron transfer and good chemical stability. The synergistic effect between $Fe_3C$ and CNTs significantly improves ORR performance. EDS mapping images reveal uniformly distributed Fe, N, and C throughout $Fe_3C@CNTs/NC-M$ (Fig. 1g-j).
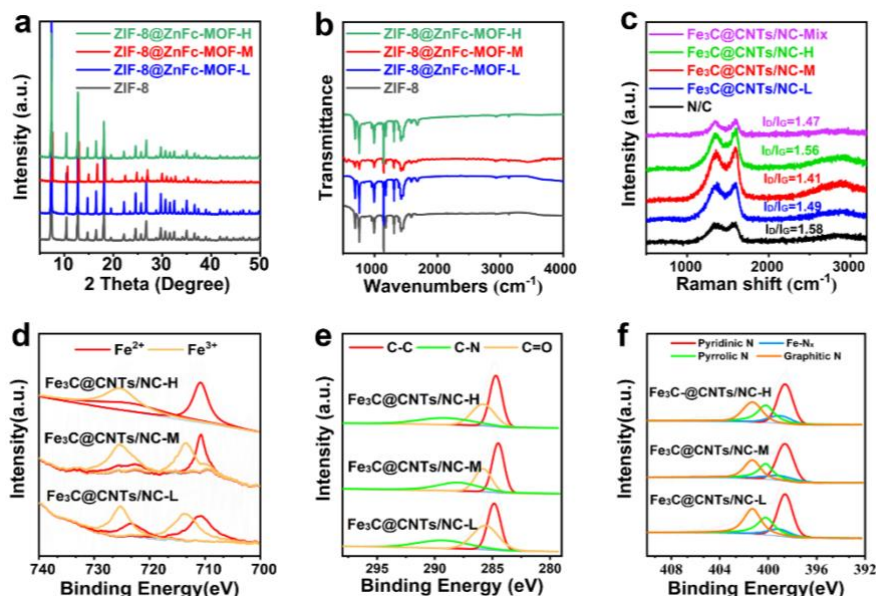
Figure 2 (a) XRD and (b) IR spectra of ZIF-8 and ZIF-8@ZnFc-MOF-M; (c) Raman spectra of Fe₃C@CNT/NC-x; High-resolution XPS spectra of the (d) Fe 2p, (e) C 1s and (f) N 1s regions of Fe₃C@CNT/NC-x

Further structural and chemical characterization of the catalysts and their precursors is presented in Fig. 2. X-ray diffraction (XRD) measurements, Fig. 2a, reveal identical patterns for ZIF-8@ZnFc-MOF-x and ZIF-8, indicating that Fe doping has no major effect on the ZIF-8 template crystal structure. The presence of FcCOOH is verified by its multiple characteristic peaks in the infrared (IR) spectrum, Fig. 2b, including at 345 $cm^{-1}$ (outside mode) and 605 $cm^{-1}$ (inside bending of ferrocene characteristic rings), at 1185 $cm^{-1}$ (bending vibration of ferrocene C-C bond), at 1300 $cm^{-1}$ (stretching vibration of ferrocene C-O bond), and at 3053 ~ 3073 $cm^{-1}$ (stretching vibration of carboxyl C-H bond). Following FcCOOH functionalization, the ZIF-8@ZnFc-MOF-x precursors were converted to Fe₃C@CNTs/NC-x catalysts by annealing at 920 °C. For comparison, also a pure NC framework was synthesized from ZIF-8 following a similar method to Fe₃C@CNTs/NC-x. The XRD spectra in Fig. S17 show that Fe₃C@CNTs/NC-x have the same wide peak (2θ) in the range of 20-30° as that of NC, while Fe₃C@CNTs/NC-Mix shows a more pronounced diffraction peak at 45° for the (1 1 0) crystal plane of Fe.

Nitrogen adsorption-desorption isotherms were determined to characterize the surface area and pore size distribution of the catalysts (Figure S18). The isotherms of our catalysts were attributed to type IV. Based on the Braeuer-Emmett-Teller (BET) method, the surface area of Fe₃C@CNTs/NC-M was determined as 844.1 $m^2/g$, with an average pore diameter of 4 nm (Figure S18). This large surface area increases contact between catalyst and $O_2$ and improves catalytic performance.

In general, carbon materials with graphitic structure and controllable defects/disorder effectively enhance electrocatalytic performance. Raman spectroscopy is a powerful technique to directly probe the extent of graphitization and the presence of symmetry-breaking defects through the intensity of the characteristic D and G bands [39]. Pristine, defect-free graphene and graphite show an intense G band yet no D band. As sp3 defects are gradually introduced, for instance by covalent grafting of radicals on a graphite surface [40,41], a D band emerges whose intensity roughly scales with the number density of defects. In the present case, the intensity ratio ID/IG value can be considered inversely proportional with the degree of graphitization: Fig. 2c shows that Fe₃C@CNTs/NC-M has the lowest ID/IG value (1.41) and thus the highest degree of graphitization, followed by Fe₃C@CNTs/NC-Mix (1.47), Fe₃C@CNTs/NC-L (1.49), Fe₃C@CNTs/NC-H (1.56) and NC (1.58). As a higher degree of graphitization and limited defects/disorder of the framework result in better electrical conductivity of Fe₃C@CNTs/NC-M, this property is expected to have a direct impact on ORR performance.

To further characterize the composition and chemical environment in the catalysts, X-ray photoelectron spectroscopy (XPS) was performed on the Fe₃C@CNTs/NC-x materials. The survey spectra in Fig. S19 confirm that N, O, C and Fe are present in Fe₃C@CNTs/NC-x. Evaluating in greater detail, three peaks occur in the high-resolution Fe 2p region in Fe₃C@CNT/NC-x, Fig. 2d and S20. The peaks at 710.8 eV and 723.0 eV correspond to $Fe^{2+}$ $2p_{3/2}$ and $Fe^{2+}$ $2p_{1/2}$ orbitals. The peaks at 713.5 eV and 725.3 eV, at slightly higher binding energies, correspond to $Fe^{3+}$ $2p_{3/2}$ and $Fe^{3+}$ $2p_{1/2}$ orbitals [42,43]. Increasing the Fe content in the catalysts changes the ratio between $Fe^{2+}$ and $Fe^{3+}$ present. Peaks at 284.5 eV, 285.8 eV and 289.1 eV, Fig. 2e and S21, in the C 1s region are attributed to C-C, C-N and C=O bonds, respectively, as the electronegativity of

the binding partner increases [44]. The peak at 285.8 eV (C-N bond) further confirms the formation of an N-doped carbon matrix. Fig. 2f and S22 indicate the co-existence of pyridinic N (398.2 eV), Fe-N (N coordinated to Fe, 399.3 eV), pyrrolic N (400.7 eV), and graphitic N (403.0 eV) in the N 1s region for Fe$_3$C@CNTs/NC-x after heat treatment [37], suggesting the presence of FeNx catalytic species. The pyridinic N affects the electronic and geometric properties of the carbon skeleton and the graphitized N group is expected to play a role in the ORR mechanism. Finally, the O 1s spectra of Fe$_3$C@CNTs/NC-L, Fe$_3$C@CNTs/NC-M, Fe$_3$C@CNTs/NC-H and NC have similar peaks at 530.9 eV, Fig. S23, and a Fe-O bond is in evidence due to the inevitable oxidation of the catalyst surface.
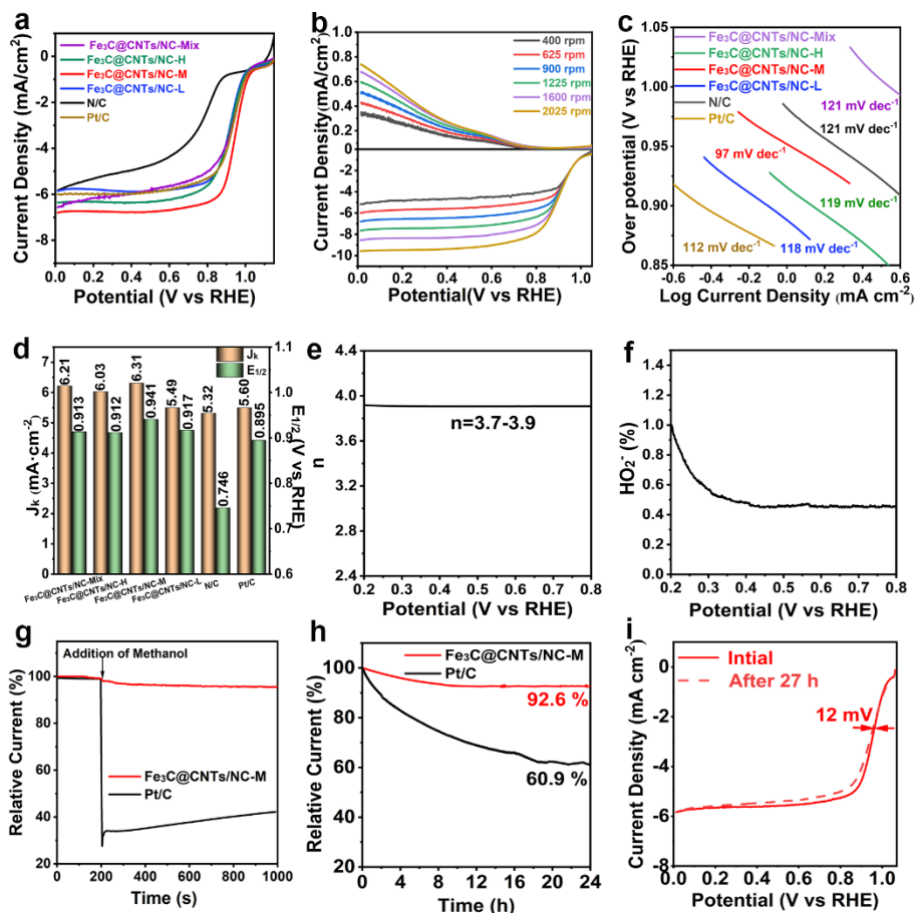


Figure 3 (a) RDE voltammograms of various Fe$_3$C@CNTs/NC-x and commercial catalysts, rotation rate 1600 rpm, potential scan rate 5 mV s$^{-1}$; (b) RRDE voltammograms of Fe$_3$C@CNTs/NC-M; the Pt ring potential was fixed at 1.5V vs RHE to oxidize any peroxide formed at the disc; rotation rates as indicated; (c) Tafel curves of various Fe$_3$C@CNTs/NC-x and commercial catalysts; (d) E$_{1/2}$ and j$_k$; (e) Number of electrons transferred; (f) H$_2$O$_2$ yield; (g) Methanol tolerance; (h) ORR current stability of Fe$_3$C@CNTs/NC-M and Pt/C over 24 h; (i) LSV of Fe$_3$C@CNTs/NC-M at 1600 rpm before and after 27 h.

Rotating disk electrode (RDE) measurements were used to investigate ORR performance of electrocatalysts in O$_2$ saturated 0.1 M KOH. Fig. 3a shows that Fe$_3$C@CNTs/NC-M has the best ORR electrocatalytic activity in terms of the half-wave potential (E$_{1/2}$) and onset potential (Eonset). The E$_{1/2}$ of Fe$_3$C@CNTs/NC-M is 0.941 V, compared to that of Pt/C (0.895 V) and the reference catalyst NC (0.746 V), suggesting that the Fe$_3$C component provides the most electroactive sites in the ORR process. Fe$_3$C and Fe-N$_x$ components provide more active sites and play an important role in ORR and improve the performance of ORR, but it is important to control the relative content of Fe$_3$C in the electrocatalyst. When the Fe$_3$C content is too low, the synergistic effect of Fe$_3$C and Fe-N$_x$ cannot reach the optimal level. When the Fe$_3$C content is high, it covers the active sites of Fe-N$_x$, thus compromising the catalytic effect [45]. Therefore controlling the relative content of the Fe$_3$C in electrocatalysts is also vital, as both lower and higher Fe$_3$C content worsens ORR performance: in Fe$_3$C@CNTs/NC-L, E$_{1/2}$ = 0.917 V while in Fe$_3$C@CNTs/NC-H, E$_{1/2}$ = 0.912 V. Covalent anchoring the Fe$_3$C nanoparticles on the NC template is also essential to achieve excellent ORR performance. Simple blending of Fe$_3$C@CNTs and NC framework in Fe$_3$C@CNTs/NC-Mix results in a poor E$_{1/2}$ = 0.913 V.

Additionally, Fig. 3d shows that $Fe_3C@CNTs/NC$-M offers the kinetic current density (6.31 mA/cm$^2$) at the half-wave potential (for the calculation, see supporting information), compared to that of Pt/C (5.60 mA/cm$^2$), $Fe_3C@CNTs/NC$-L (5.50 mA/cm$^2$), $Fe_3C@CNTs/NC$-H (6.03 mA/cm$^2$), and $Fe_3C@CNTs/NC$-Mix (6.22 mA/cm$^2$). Table S2 shows that $Fe_3C@CNTs/NC$-M surpasses the performance of most documented non-noble metal-based ORR electrocatalysts. Fig. 3b and S24-S27 show RDE measurements for $Fe_3C@CNTs/NC$-x as a function of rotation rate. Tafel slope is a crucial criterion for judging the reaction kinetics of ORR electrocatalysts. Fig. 3c shows that $Fe_3C@CNTs/NC$-M has the fastest reaction kinetics, based on the smallest Tafel slope (97 mV dec$^{-1}$), in comparison with that of NC (121 mV dec$^{-1}$), $Fe_3C@CNTs/NC$-L (118 mV dec$^{-1}$), $Fe_3C@CNTs/NC$-H (119 mV dec$^{-1}$), $Fe_3C@CNTs/NC$-Mix (121 mV dec$^{-1}$) and Pt/C (112 mV dec$^{-1}$).

In order to analyze the product formed at the disk, rotating ring-disk measurements were performed with the disk held at 1.5V, where any peroxide is oxidized in a mass-transport-limited manner, Fig.3b top panel. The number of electrons transferred n close to 4 (Fig. 3e) and the calculated $H_2O_2$ yield remaining below 1.0 % (Fig. 3f) for $Fe_3C@CNTs/NC$-M confirm that water is produced quantitatively in the entire potential range from 0.2 to 0.8 V.

The activity of catalysts is closely related to its electrochemical active surface area (ECSA). A large ECSA increases accessibility of active sites and promotes the catalysed reaction. In this case, the ECSA of different catalysts was assessed by evaluating the double-layer capacitance ($C_{dl}$). As can be seen from Figure S28, the $C_{dl}$ value of $Fe_3C@CNTs/NC$-M (0.00362 mF cm$^{-2}$) is higher than that of NC (0.00134 mF cm$^{-2}$), $Fe_3C@CNTs/NC$-L (0.00190 mF cm$^{-2}$), $Fe_3C@CNTs/NC$-H (0.00308 mF cm$^{-2}$), $Fe_3C@CNTs/Nc$-Mix (0.0093 mF cm$^{-2}$), suggesting that $Fe_3C@CNTs/NC$-M provides highest access to active sites. In addition, electrochemical impedance spectroscopy (EIS) was used to determine the charge transfer resistance (Figure S29). It can be clearly seen that $Fe_3C@CNTs/NC$-M has a smaller charge transfer resistance than that of NC, $Fe_3C@CNTs/NC$-L, $Fe_3C@CNTs/NC$-H and $Fe_3C@CNTs/NC$-Mix, in accordance with its highest catalytic activity.

Long-term durability and solvent tolerance are important criteria for the practical evaluation of catalyst performance. Fig. 3g shows that the addition of 1 mL methanol at 200 s barely changes the ORR relative current density of $Fe_3C@CNTs/NC$-M, while the commercial Pt/C catalyst rapidly loses electrocatalytic activity, proving considerable methanol tolerance for $Fe_3C@CNTs/NC$-M. Notably, the chronoamperometric measurements at 0.8 V show that $Fe_3C@CNTs/NC$-M has 92.6 % current retention after 24 h, compared to 60.9 % for Pt/C, Fig. 3h. Additionally, the loss of $J_k$ and $E_{1/2}$ value of $Fe_3C@CNTs/NC$-M is negligible after continuous 27 h operation, Fig. 3i. These results prove that $Fe_3C@CNTs/NC$-M is a competitive electrocatalyst for ORR with high electrocatalytic activity, durability and high methanol tolerance in alkaline electrolytes.
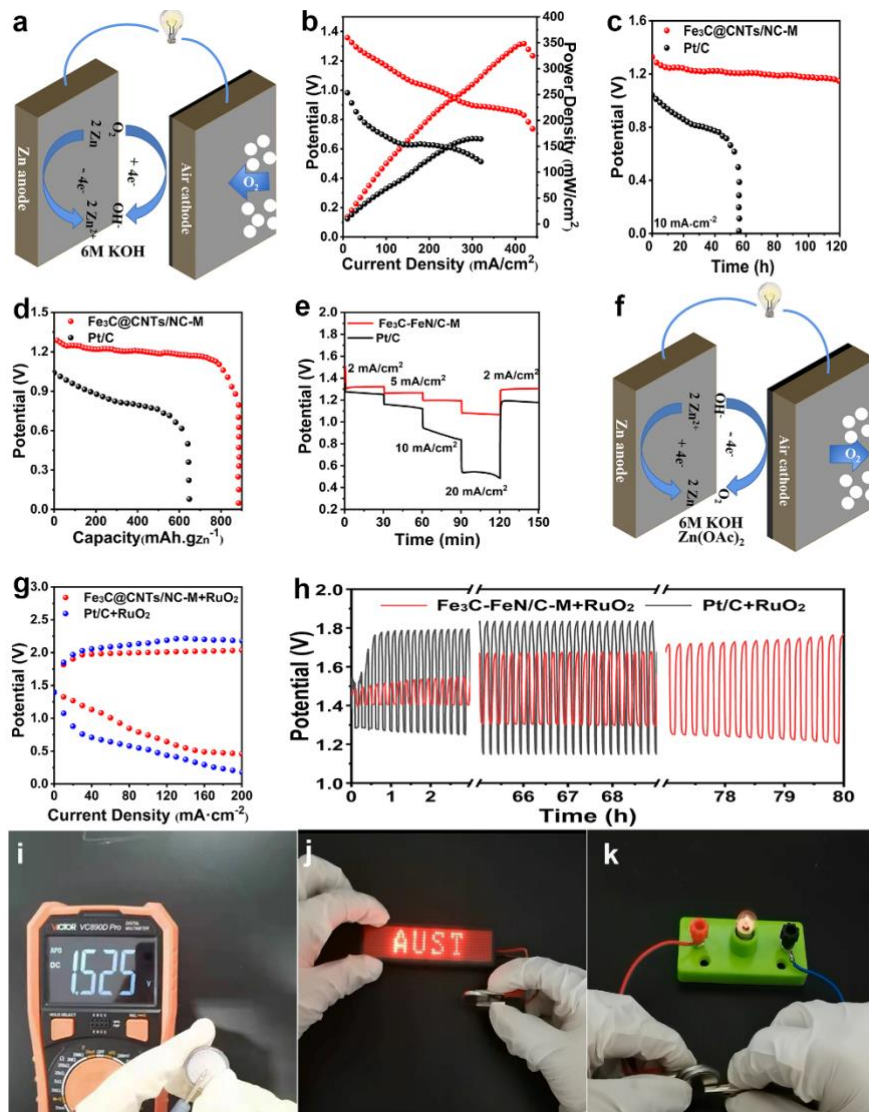
Figure 4 (a) Schematic illustration of the discharge process of a primary ZAB; (b) Power density and polarization curve of the ZAB; (c) Long-time constant current discharge curve of Fe₃C@CNTs/NC-M and Pt/C as air electrodes in the ZAB; (d) Specific discharge capacity of Fe₃C@CNTs/NC-M and Pt/C as air electrodes in the ZAB; (e) Discharge curve of the ZAB with varying rate performance; (f) Secondary ZAB charge/discharge cycle; (g) Comparison of charge/discharge curves using Fe₃C@CNTs/NC-M+RuO₂ and Pt/C+RuO₂ cathodes; (h) Cycling performance at a current density of 1 mA/cm²; (i) The OCV of Fe₃C@CNTs/NC-M//RuO₂ ZAB; Photograph of (j) miniature LED display and (k) small light bulb powered by the Fe₃C@CNTs/NC-M//RuO₂ ZAB.

The performance of Fe₃C@CNTs/NC-M was further evaluated as an oxygen electrode in a primary zinc-air battery (ZAB) (Fig. 4a and S30). The Fe₃C@CNTs/NC-M ZAB generates excellent peak power density (348 mW/cm² at 420 mA/cm²), which far surpasses that of Pt/C ZAB (164 mW/cm² at 300 mA/cm²), Fig. 4b. The Fe₃C@CNTs/NC-M ZAB shows high electrocatalytic stability, with only 8.8% decay with respect to the initial voltage (1.260 V) after a continuous 56 h test, compared to that of Pt/C ZAB with a sharp voltage drop (from 1.040 V to 0 V), Fig. 4c. recoverability.

To test the reliability and practicability of

Besides, the Fe₃C@CNTs/NC-M ZAB achieved 843 mAh/g$_{Zn}$⁻¹ maximum specific capacity at 10 mA/cm², compared to that of Pt/C (652 mAh/g$_{Zn}$⁻¹), Fig. 4d. To further evaluate the rate performance, current density dependent (from 2 to 20 mA/cm²) discharge curves are shown in Fig. 4e. The Fe₃C@CNTs/NC-M ZAB only shows 1.0 % voltage drop after the rate discharge test, with a steady platform under all discharge current densities, which much exceeds the Pt/C ZAB, Fig. 4e. These results suggest that Fe₃C@CNTs/NC-M is a promising ZAB cathode with excellent durability and Fe₃C@CNTs/NC-M in rechargeable ZABs, Fe₃C@CNTs/NC-M + RuO₂ (1:1) are combined as the air

electrode and tested in 6.0 M KOH and 0.2 M $Zn(Ac)_2$ (Fig. 4f and S30). The $Fe_3C@CNTs/NC-M//RuO_2$ ZAB shows much lower voltage than that observed in $Pt/C//RuO_2$ ZAB during cycling, Fig. 4g. Fig. 4h shows that the $Fe_3C@CNTs/NC-M//RuO_2$ ZAB has a small $\Delta E$ (0.12 V) at 1 $mA/cm^2$ with the initial charging potential at 1.58 V and discharging potential at 1.46 V, respectively. After 70 h continuous test, these values change to 1.68 V and 1.31 V, which outperforms $Pt/C//RuO_2$ ZAB (initial: 1.80/1.24 V, after 70 h: 1.84/1.16 V). Furthermore, $Fe_3C@CNTs/NC-M//RuO_2$ ZAB still functions well after 80 h of continuous testing, with its charging and discharging potentials at 1.73 and 1.24 V ($\Delta E$ = 0.49 V), respectively. The whole durability test outlasted > 200 h, Fig. S31.

A portable power supply was also fabricated to demonstrate the practical use of the $Fe_3C@CNTs/NC-M$ ZAB, wich showed a satisfactory 1.525 V open-circuit voltage (Fig. 4i). Furthermore, the $Fe_3C@CNTs/NC-M$ ZAB can provide sufficient output to power a miniature light-emitting diode (LED) display and a miniature light bulb (Fig. 4j and Fig. 4k).

## CONCLUSIONS

In summary, we have investigated the synergistic effect of Fe-containing nanoparticles, N-doped carbon matrix and CNTs on the ORR performance without the interference of other metal elements. Specifically, FcCOOH modified ZIF-8 was successfully prepared by in-situ ligand substitution. Upon further high-temperature carbonization, ORR electroactive $Fe_3C$ nanoparticles were generated by the reduction of $Fe^{2+}$ and encapsulated in CNTs, and FeNx doped porous carbon material was formed as the template matrix. The synthetic effect of both $Fe_3C$ nanoparticles and FeNx doped porous carbon material was demonstrated as the most critical part for the improvement of electrocatalytic ORR properties. CNTs coating was believed to promote the solvent tolerance, durability and electrocatalytic activity. The optimized catalyst $Fe_3C@CNTs/NC-M$ displays advanced ORR activity with excellent $E_{1/2}$ at 0.941 V, and outstanding limiting current density at 6.31 $mA/cm^2$, along with strong resistance towards methanol poisoning and long-term durability. The $Fe_3C@CNTs/NC-M$ ZAB also exhibits an outstanding power density (348 $mW/cm^2$) and excellent OCV (1.525 V). This work further develops a feasible ligand substitution and pyrolysis strategy for studying CNTs coated single metallic electrocatalysts without interference of other metal elements for zinc-air battery applications.

## REFERENCES

1. Zhao T, Wu H, Wen X, et al. Recent advances in MOFs/MOF derived nanomaterials toward high-efficiency aqueous zinc ion batteries. *Coord Chem Rev.* 2022;468:214642.

2. Qin X, Kim D, Piao Y. Metal‐organic frameworks‐derived novel nanostructured electrocatalysts for oxygen evolution reaction. *Carbon Energy.* 2020;3:66-100.

3. Li S, Li E, An X, Hao X, Jiang Z, Guan G. Transition metal-based catalysts for electrochemical water splitting at high current density: current status and perspectives. *Nanoscale.* 2021;13:12788-12817.

4. Shen Y, Pan T, Wang L, Ren Z, Zhang W, Huo F. Programmable Logic in Metal-Organic Frameworks for Catalysis. *Adv Mater.* 2021;33:e2007442.

5. Hu J, Xu Q, Wang X, et al. Charge‐transfer‐regulated bimetal ferrocene‐based organic frameworks for promoting electrocatalytic oxygen evolution. *Carbon Energy.* 2023:DOI: 10.1002/cey1002.1315.

6. Zhao M, Liu H, Zhang H, et al. A pH-universal ORR catalyst with single-atom iron sites derived from a double-layer MOF for superior flexible quasi-solid-state rechargeable Zn–air batteries. *Energy Environ Sci.* 2021;14:6455-6463.

7. Deng Y, Chi B, Li J, et al. Atomic Fe‐Doped MOF‐Derived Carbon Polyhedrons with High Active‐Center Density and Ultra‐High Performance toward PEM Fuel Cells. *Adv Energy Mater* 2019;9:1802856.

8. Li Y, Zhang P, Wan L, et al. A General Carboxylate‐Assisted Approach to Boost the ORR Performance of ZIF‐Derived Fe/N/C Catalysts for Proton Exchange Membrane Fuel Cells. *Adv Funct Mater.* 2021;31:2009645.

9. Li C, Zhang H, Liu M, Lang F-F, Pang J, Bu X-H. Recent progress in metal–organic frameworks (MOFs) for electrocatalysis. *Ind Chem Mater.* 2023;1:9-38.

10. Kandambeth S, Kale VS, Fan D, et al. Unveiling Chemically Robust Bimetallic Squarate‐Based Metal–Organic Frameworks for Electrocatalytic Oxygen Evolution Reaction. *Adv Funct Mater.* 2022;13:2202964.

11. Pan J, Chen Z, Wang P, et al. The overall water splitting of $CdS/Ti^{3+}-SrTiO_3$ core–shell heterojunction via OER enhancement of MnOx nanoparticles. *Chem Eng J.* 2021;424:130357.

12. Yuan S, Cui LL, Dou Z, et al. Nonprecious Bimetallic Sites Coordinated on N-Doped Carbons with Efficient and Durable Catalytic Activity for Oxygen Reduction. *Small.* 2020;16:2000742.

13. Zhang X, Zhang S, Yang Y, et al. A General

Method for Transition Metal Single Atoms Anchored on Honeycomb-Like Nitrogen-Doped Carbon Nanosheets. *Adv Mater.* 2020;32:1906905.

14. Cao L, Li Z, Su K, Zhang M, Cheng B. Rational design of hollow oxygen deficiency-enriched $NiFe_2O_4$@N/rGO as bifunctional electrocatalysts for overall water splitting. *J Energy Chem.* 2021;54:595-603.

15. Chen C, Tuo Y, Lu Q, et al. Hierarchical trimetallic Co-Ni-Fe oxides derived from core-shell structured metal-organic frameworks for highly efficient oxygen evolution reaction. *Appl Catal B Environ.* 2021;287:119953.

16. Jin H, Zhao X, Liang L, et al. Sulfate Ions Induced Concave Porous S‐N Co‐Doped Carbon Confined $FeCx$ Nanoclusters with Fe‐$N_4$ Sites for Efficient Oxygen Reduction in Alkaline and Acid Media. *Small.* 2021;17.

17. Zhang L, Zhu J, Li X, et al. Nurturing the marriages of single atoms with atomic clusters and nanoparticles for better heterogeneous electrocatalysis. *Interdisciplinary Materials.* 2022;1:51-87.

18. Wang Y, Pan Y, Zhu L, et al. Solvent-free assembly of Co/Fe-containing MOFs derived N-doped mesoporous carbon nanosheets for ORR and HER. *Carbon.* 2019;146:671-679.

19. Chen G, Liu P, Liao Z, et al. Zinc-Mediated Template Synthesis of Fe-N-C Electrocatalysts with Densely Accessible Fe-$N_x$ Active Sites for Efficient Oxygen Reduction. *Adv Mater.* 2020;32:e1907399.

20. Wang CP, Lin YX, Cui L, Zhu J, Bu XH. 2D Metal-Organic Frameworks as Competent Electrocatalysts for Water Splitting. *Small.* 2023;19:e2207342.

21. Jin H, Yu R, Hu C, et al. Size-controlled engineering of cobalt metal catalysts through a coordination effect for oxygen electrocatalysis. *Appl Catal B Environ.* 2022;317.

22. Zhao X, He X, Chen B, Yin F, Li G. MOFs derived metallic cobalt-zinc oxide@nitrogen-doped carbon/carbon nanotubes as a highly-efficient electrocatalyst for oxygen reduction reaction. *Appl Surf Sci.* 2019;487:1049-1057.

23. Zeng K, Zheng X, Li C, et al. Recent Advances in Non‐Noble Bifunctional Oxygen Electrocatalysts toward Large‐Scale Production. *Adv Funct Mater.* 2020;30:2000503.

24. Liang X, Xiao J, Weng W, Xiao W. Electrochemical Reduction of Carbon Dioxide and Iron Oxide in Molten Salts to $Fe/Fe_3C$

Modified Carbon for Electrocatalytic Oxygen Evolution. *Angew Chem Int Ed Engl.* 2021;60:2120-2124.

25. Zhao Y, Zhang J, Guo X, et al. $Fe_3C$@nitrogen doped CNT arrays aligned on nitrogen functionalized carbon nanofibers as highly efficient catalysts for the oxygen evolution reaction. *J Mater Chem A* 2017;5:19672-19679.

26. Cao M, Liu Y, Sun K, et al. Coupling $Fe_3C$ Nanoparticles and N-Doping on Wood-Derived Carbon to Construct Reversible Cathode for Zn-Air Batteries. *Small.* 2022;18:2202014.

27. Yang Q, Liu R, Pan Y, et al. Ultrahigh-Loaded Fe Single Atoms and $Fe_3C$ Nanoparticle Catalysts as Air Cathodes for High-Performance Zn-Air Batteries. *ACS Appl Mater Interfaces.* 2023;15:5720-5731.

28. Xu W, Yoon D, Yang Y, et al. MOF-Derived Bimetallic Pd-Co Alkaline ORR Electrocatalysts. *ACS Appl Mater Interfaces.* 2022;14:44735-44744.

29. Cheng H, Xu G, Zhu C, Alhalili Z, Du X, Gao G. Porous MOF derived $TiO_2$/ZnO/C@CNTs composites for enhancing lithium storage performance. *Chem Eng J.* 2023;454:140454.

30. Liu X, Wang L, Zhang G, et al. Zinc assisted epitaxial growth of N-doped CNTs-based zeolitic imidazole frameworks derivative for high efficient oxygen reduction reaction in Zn-air battery. *Chem Eng J.* 2021;414:127569.

31. Choi EY, Kim DE, Lee SY, Park CB, Kim CK. Cobalt nanoparticles-encapsulated holey nitrogen-doped carbon nanotubes for stable and efficient oxygen reduction and evolution reactions in rechargeable Zn-air batteries. *Appl Catal B Environ.* 2023;325:122386.

32. Luo W, Wang Y, Luo L, et al. Single-Atom and Bimetallic Nanoalloy Supported on Nanotubes as a Bifunctional Electrocatalyst for Ultrahigh-Current-Density Overall Water Splitting. *ACS Catalysis.* 2022;12:1167-1179.

33. Xue J, Deng S, Wang R, Li Y. Efficient synergistic effect of trimetallic organic frameworks derived as bifunctional catalysis for the rechargeable zinc-air flow battery. *Carbon.* 2023;205:422-434.

34. Li S, Feng C, Xie Y, Guo C, Zhang L, Wang J. Synthesis of nitrogen-rich porous carbon nanotubes coated Co nanomaterials as efficient ORR electrocatalysts via MOFs as precursor. *J Alloys Compd.* 2022;911:165060.

35. Srinivas K, Chen X, Liu D, et al. Surface modification of metal-organic frameworks under sublimated iron-atmosphere by controlled carbonization for boosted oxygen

evolution reaction. *Nano Res.* 2022;15:5884-5894.

36. Zhang S, Lin C, Ye J, et al. $Bi_2S_3$/rGO nanocomposites with covalent heterojunctions as a high-performance aqueous zinc ion battery material. *Ceramics International.* 2023;49:22160-22169.

37. Ruan QD, Feng R, Feng JJ, Gao YJ, Zhang L, Wang AJ. High-Activity $Fe_3C$ as pH-Universal Electrocatalyst for Boosting Oxygen Reduction Reaction and Zinc-Air Battery. *Small.* 2023:2300136.

38. Cheng Y, Hu S, Luo G, Gao Z, Zhang X. FeCoN Co-doped Hollow Carbon Nanocage Grafted with Carbon Nanotubes as an Electrocatalyst for Enhanced Oxygen Reduction Reaction. *ACS Appl Energy Mater.* 2023;6:2010-2021.

39. C. A, Ferrari1, Basko DM. Raman spectroscopy as a versatile tool for studying the properties of graphene. *Nat Nanotechnol.* 2013;8:235-246.

40. Phan TH, Van Gorp H, Li Z, et al. Graphite and Graphene Fairy Circles: A Bottom-Up Approach for the Formation of Nanocorrals. *ACS Nano.* 2019;13:5559-5571.

41. Greenwood J, Phan TH, Fujita Y, et al. Covalent Modification of Graphene and Graphite Using Diazonium Chemistry: Tunable Grafting and Nanomanipulation. *ACS Nano.* 2015;5:5520-5535.

42. Li YW, Zhang WJ, Li J, et al. Fe-MOF-Derived Efficient ORR/OER Bifunctional Electrocatalyst for Rechargeable Zinc-Air Batteries. *ACS Appl Mater Interfaces.* 2020;12:44710-44719.

43. Xie T, Hu J, Xu Q, Zhou C. Metal-organic framework derived $Fe_3C$ nanoparticles coupled single-atomic iron for boosting oxygen reduction reaction. *J Colloid Interface Sci.* 2023;630:688-697.

44. Ding J, Guo D, Hu A, et al. Resisting metal aggregation in pyrolysis of MOFs towards high-density metal nanocatalysts for efficient hydrazine assisted hydrogen production. *Nano Res.* 2022:10.1007/s12274-12022-14777-12275.

45. Xu C, Guo C, Liu J, et al. Accelerating the oxygen adsorption kinetics to regulate the oxygen reduction catalysis via $Fe_3C$ nanoparticles coupled with single $Fe-N_4$ sites. *Energy Storage Mater.* 2022;51:149-158.

**Author contributions** Cuiping Wang: Writing - original draft and experimental design, Jinsong Hu: Administration and Writing - review & editing, Zhi Li: Writing - review & editing, Stijn F. L. Mertens: Writing - review & editing, Jie Lei and Song Li: Data processing.

**Conflict of interest** The authors declare that they have no conflict of interest.

**Supplementary information** Experimental details and supporting data are available in the online version of the paper.



**Cuiping Wang** is a master student at the School of Chemical Engineering, Anhui University of Science and Technology. Her main research interest is the application of metal-organic frame materials and their derivatives in electrochemistry



**Zhi Li** received the Ph.D. degree in 2017 in the department of Chemistry of KU Leuven under supervision of Prof. Steven De Feyter and Prof. Stijn F. L. Mertens. Afterwards, he joined Nanjing university as a postdoctoral fellow in 2019. He joined Anhui University of Science and Technology(AUST) in 2022 with research interests including functionalization of 2D materials, electrocatalytic processes.

**Stijn F. L. Mertens** is Professor of Physical Electrochemistry at Lancaster University, UK. He obtained a PhD in chemistry from Ghent University, Belgium, and a Habilitation in chemical physics from the Vienna University of Technology, Austria. His research interests include in situ and in operando studies of well-defined electrochemical interfaces towards an atomic-scale understanding of catalysis, molecular self-assembly and single-molecule switching.



**Jinsong Hu** received the Ph.D. degree in 2011, then he worked at Anhui University of Science and Technology(AUST). After a postdoctoral career at AUST from November 2015 to August 2017, he began independent research as a Professor at AUST. His research interests include fluorescent sensor of metal-organic frameworks(MOFs) and MOFs-based nano materials.

<span style="color:red">氮碳包封 $Fe_3C$ 纳米颗粒作为高效富氧还原电催化剂</span>

汪翠萍 1, 李智 1*, 雷杰 1, 李松 1, Stijn F. L. Mertens 2*, 胡劲松 1,3*

**摘要** 高活性 MOF 基催化剂的设计和合成为促进动力学不利的氧还原反应(ORR)过程开辟了新的途径。本研究通过在 ZIF-8 前驱体表面涂覆二茂铁甲酸，然后进行两步炭化工艺，设计和制备了一种新型结构的高效电催化剂，以提高 ORR 性能，这对于将热解 Fe$_3$C 纳米颗粒封装到碳纳米管(CNTs)中以及将 Fe 单原子隔离到 N 掺杂碳(NC)基体上至关重要。此外，Fe 元素的相对含量对优化催化剂的 ORR 性能至关重要。所制得 Fe$_3$C@CNTs/NC-M 催化剂结构先进，在碱性溶液中表现出良好的长期稳定性和电催化 ORR 性能，其半波电位和极限电流分别达到 0.941V 和 6.31 mA/cm$^2$。此外，该电催化剂在甲醇溶液中具有较强的耐受性和良好的稳定性。Fe$_3$C@CNTs/NC-M 锌空气电池(ZAB)具有 1.525 V 的开路电位，420 mA/cm$^2$ 时的峰值功率密度为 348 mW/cm$^2$, 10 mA/cm$^2$ 时的最大容量为 843 mAh/g·$_{zn}$$^{-1}$。因此，这种合成策略为构建具有有效和稳定的 ORR 性能的 MOF 基电催化材料提供了一条有希望的途径。

# Nitrogen-carbon-encapsulated Fe₃C nanoparticles as highly efficient earth-abundant oxygen reduction electrocatalysts

Cuiping Wang [1], Zhi Li [1*], Jie Lei [1], Song Li [1], Stijn F. L. Mertens [2*], Jinsong Hu [1, 3*]

[1] *School of Chemical Engineering, Anhui Province Key Laboratory of Specialty Polymers, Anhui University of Science and Technology, Huainan 232001, China*

[2] *Department of Chemistry, Energy Lancaster and Materials Science Lancaster, Lancaster University, Lancaster LA1 4YB, United Kingdom*

[3] *Institute of Energy, Hefei Comprehensive National Science Center, Anhui, Hefei 230031, China*

[†] *Present address: School of Chemical Engineering, Anhui University of Science and Technology, Huainan 232001, China*

## 1 Materials

Zinc (II) nitrate hexahydrate (Zn(NO₃)₂·6H₂O, Sinopharm), 2-methylimidazole, N,N-dimethylformamide (DMF, Enox), ferrocenecarboxylic acid (FcCOOH, Enox), concentrated sulfuric acid (H₂SO₄, 98.0 %, Shanghai Zhenqi Chemical Reagent Co., Ltd.), potassium hydroxide (KOH, Enox), absolute methanol, absolute ethanol (Enox), Nafion solution (5 wt. %, Sigma-Aldrich), commercial Pt/C (20 wt. %, Sigma-Aldrich) and RuO₂ (Sigma-Aldrich) were of analytical grade and used as received.

## 2 Materials characterization

The composition and crystalline phase of the sample were investigated with powder X-ray diffraction measurements (XRD, Shimadzu XRD-6000, Japan), X-ray photoelectron spectroscopy (XPS, Thermo ESCALAB 250XI, USA), as well as energy dispersive spectrometry (EDS, Hitachi S-4800 and JEM-2100, Japan). The morphology and microstructure of the product were observed with a scanning electron microscope (SEM, Hitachi S-4800, Japan), a high-resolution transmission electron microscope/scanning transmission electron microscope (TEM/STEM, JEM-2100, Japan). Raman spectra were recorded in the spectral range of 50-3200 cm⁻¹ using a Raman microscope (LabRAM HR800, Horiba Jobin Yvon, France). FT-IR spectra were recorded for KBr-diluted samples using a Nicolet Magna 750 IR spectrometer at wavenumbers of 400-4000 cm⁻¹. Thermogravimetric analysis (TGA) was performed on a Perkin Elmer Pyris 1 TGA up to 1023 K at a heating rate of 10 K/min under N₂ atmosphere. Inductively coupled plasma optical emission spectroscopy (ICP-OES) was performed on an Agilent 5110 instrument using iron's emission wavelength of 238.204 nm, and concentration standards were prepared using Agilent standard solution (5 ppm), yielding a calibration curve with a linearity over 0.999. The samples were digested using HNO₃. Brunauer-Emmett-Teller (BET) and Barrett-Joyner-Halenda (BJH) methods were applied to determine specific surface area and pore size distribution.

Electrochemical characterization. Each catalyst (10 mg) was dispersed in a mixture of 1920 μL ethanol/H₂O (1/1, v/v) and 80 μL Nafion (5 wt. %) by ultrasonication. The ORR performances were evaluated using a CHI760D electrochemical analyzer using a standard three-electrode system. The glassy carbon electrode after loading the catalyst was used as the working electrode. A carbon rod was used as the counter electrode. A saturated calomel electrode (SCE) was selected as the reference electrode. For ORR measurements, the dispersion (10 μL) was uniformly dropcast onto a freshly polished glassy carbon electrode (4 mm diameter), and left to dry under ambient conditions. The electrochemical experiments were carried out in 0.1 M KOH electrolyte saturated with O₂ (>99.999%, Chenhong). The potential was cycled 3 times until reproducible CVs were obtained as shown in the text. Current densities were calculated using the geometric electrode surface area and the measured potential vs. SCE was converted to the reversible hydrogen electrode (RHE) scale. Rotating disk electrode (RDE, Taizhou Corete Analytical Instruments) measurements were conducted at rotating speeds between 400 and 2025 rpm, and rotating ring disk electrode (RRDE) (ca. 0.1256 cm² for disk and ca. 0.0707 cm² for the ring) measurements were carried out at 1600 rpm.

The potentials vs. SCE were converted to reversible hydrogen electrode (RHE) scale using

$$E_{RHE} = E_{SCE} + 0.0591pH + 0.244 \qquad (1)$$

The electron transfer number n was determined from RRDE measurements using disk current Id and ring current Ir via [1]

$$n = 4 \times I_d/(I_d + I_r/N) \qquad (2)$$

and the peroxide percentage % $HO_2^-$ via[1]

$$\% \ HO_2^- = 200 \times (I_r/N)/(I_d + I_r/N) \qquad (3)$$

where N=0.37 is the collection efficiency of the Pt ring.

The kinetic current was calculated from the mass-transport correction of RDE data using:

$$j_k = j \times j_L/(j_L\text{-}j) \qquad (4)$$

The electrochemically active surface area (ECSA) was estimated from the electrochemical double-layer capacitance. The double layer capacitance (Cdl) was determined with a simple CV method. CV experiments were conducted at room temperature in 0.1 M KOH solution saturated with $N_2$. Stable voltammogram curves were recorded after scanning for 10 cycles and scan rate was 100, 200, 300, 400, and 500 mV $s^{-1}$ in a narrow non-Faraday reaction part to calculate Cdl. The double-layer capacitance (Cdl) was calculated from the plot of the current density against the scan rate and the ECSA is then calculated from the double-layer capacitance according to equation (5):

$$ECSA=Cdl/C_s \qquad (5)$$

where $C_s$ is the capacitance of an atomically smooth planar surface of the material per unit area under identical electrolyte conditions.

The electrochemical impedance spectroscopy (EIS) was conducted in the frequency range of $10^5$ to 0.01 Hz with an AC amplitude of 5 mV.

For zinc–air battery experiments, Ni foams were carefully washed with 1M HCl and then rinsed with absolute ethanol and distilled water to remove oxides from the surface. The same catalyst inks as used for R(R)DE measurements were carefully dropped onto the Ni foam and then kept in a vacuum container for 30 min. For the primary Zn-air battery, the loadings of the catalyst and Pt/C were both 0.5 mg/cm². For the rechargeable Zn-air battery, the loading of the catalyst was 0.5 mg/cm², while the Pt/C and $RuO_2$ inks were mixed in a 1:1 ratio and a total catalyst loading of 0.5 mg/cm² was obtained. The Zn-air battery was assembled with Zn powder, a 6 M KOH solution (mixed with 0.2 M Zn(Ac)₂ for rechargeable Zn-air battery), and an air cathode comprising a catalyst layer and gas-diffusion layer was used as a backing layer next to the Ni foam-based catalyst layer to prevent electrolyte leakage.

## 3 Supplementary data
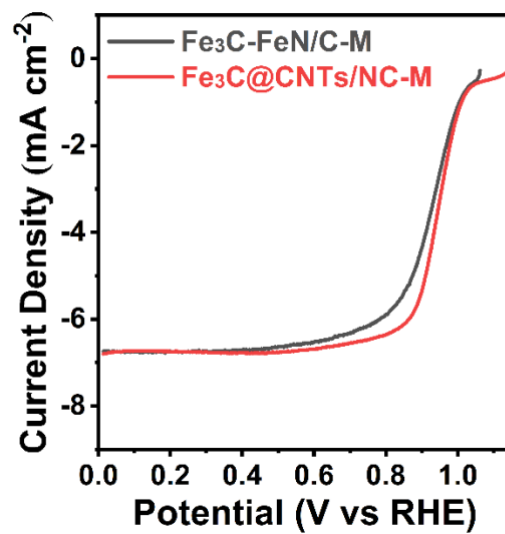


**Figure S1** LSVs of Fe$_3$C@FeN/C-M and Fe$_3$C@CNTs/NC-M in O$_2$ saturated 0.1 M KOH, 5 mV/s scan rate and 1600 rpm.
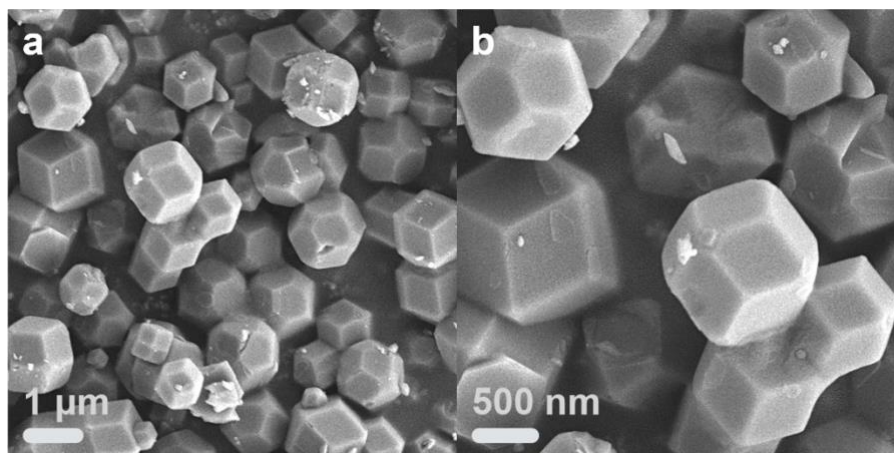


**Figure S2** SEM images of ZIF-8.
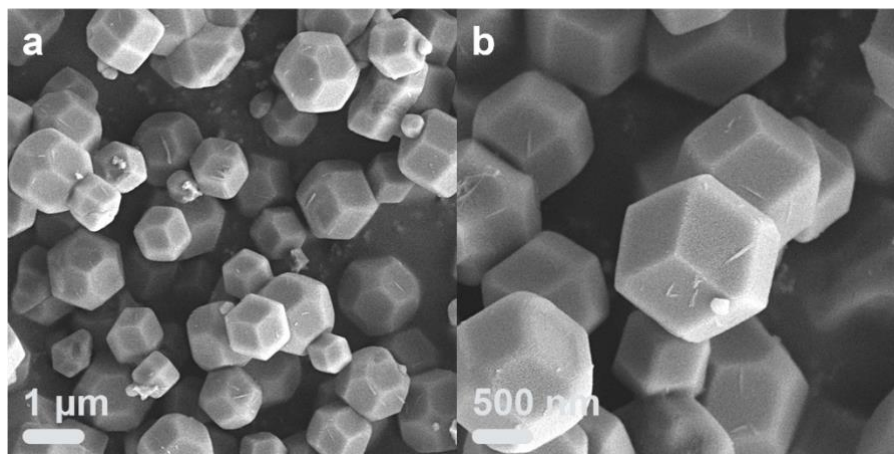
**Figure S3** SEM images of ZIF-8@ZnFc-MOF-L.
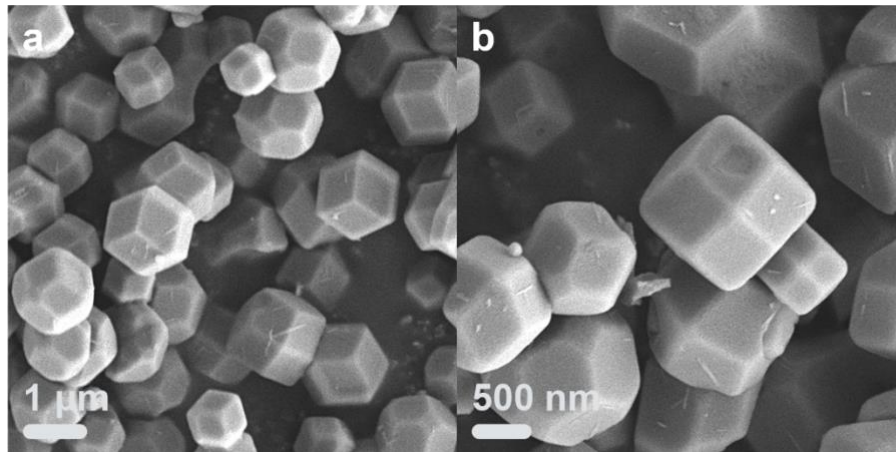


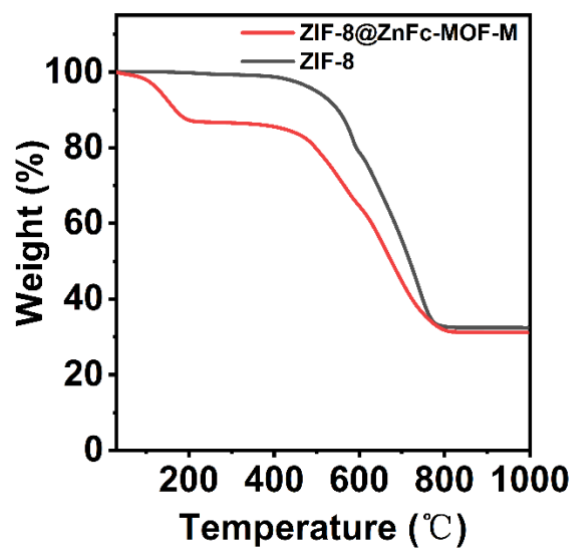**Figure S4** SEM images of ZIF-8@ZnFc-MOF-M.
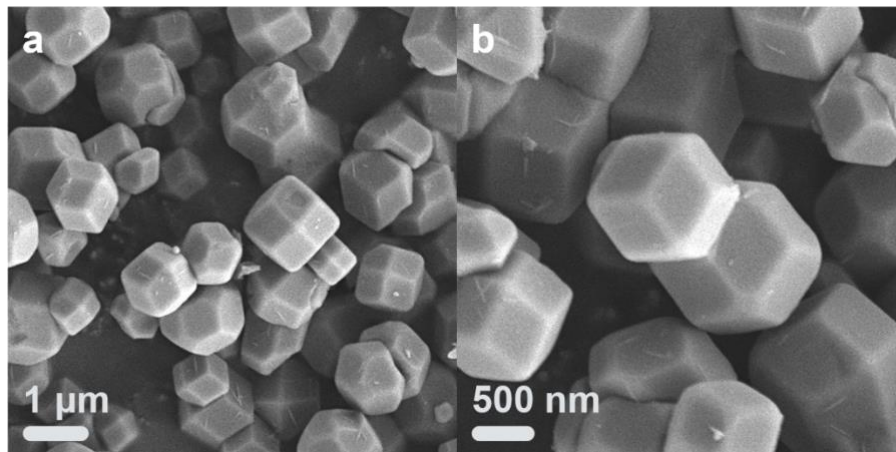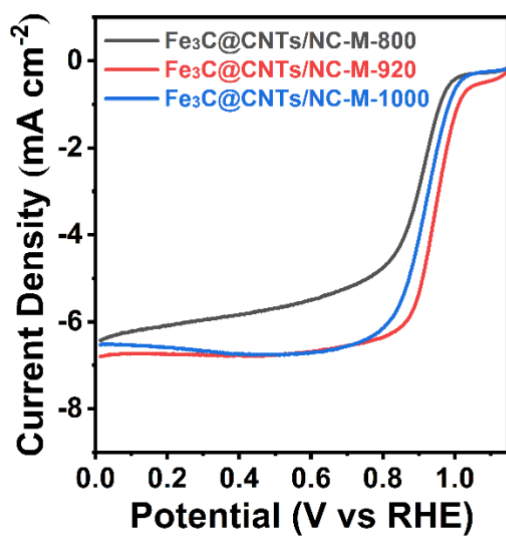


**Figure S5** SEM images of ZIF-8@ZnFc-MOF-H.
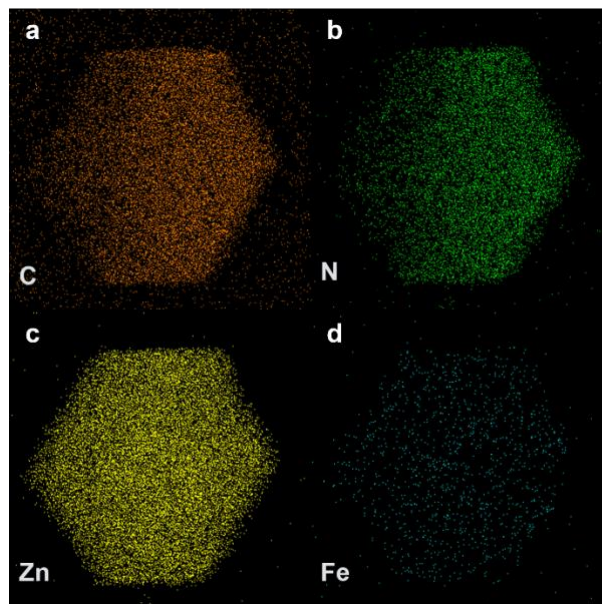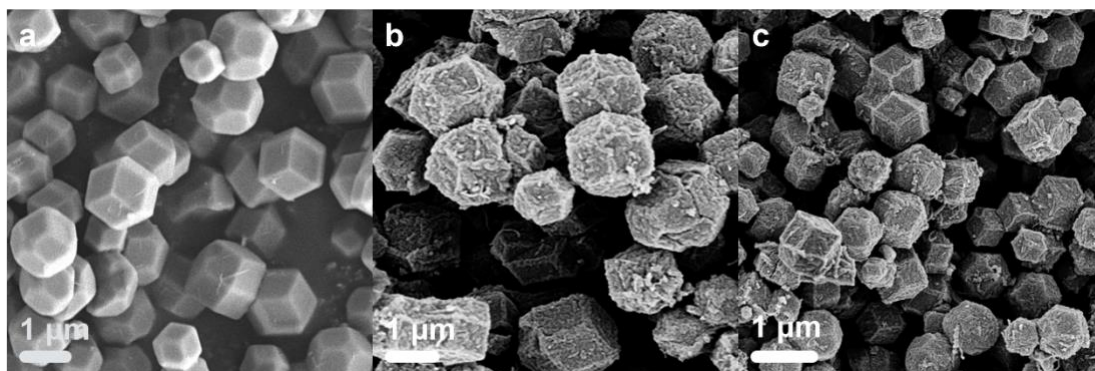


**Figure S6** EDS mapping of ZIF-8@ZnFc-MOF-M.
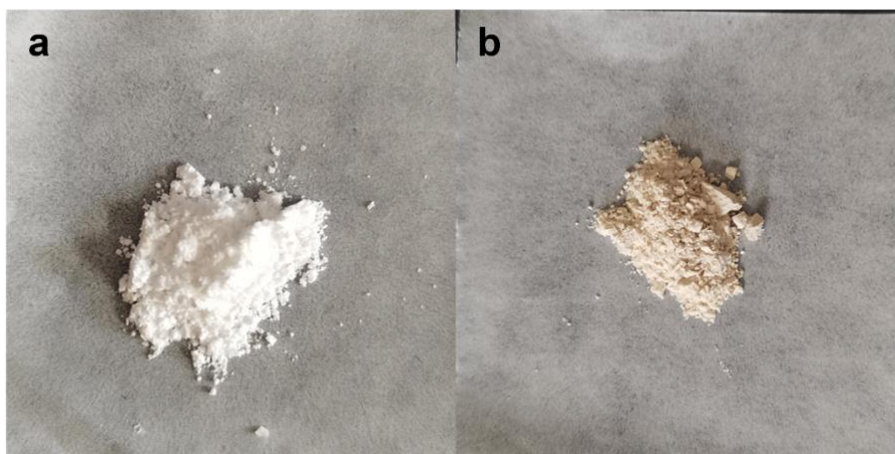
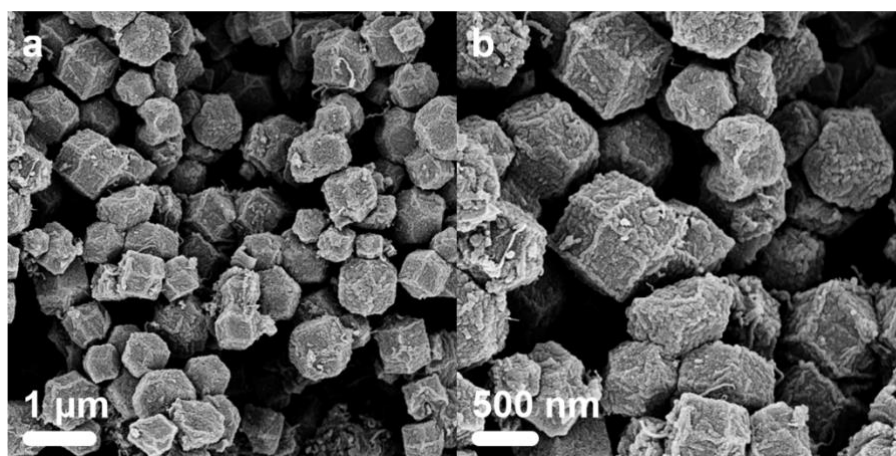**Figure S7** Visual appearance of (a) ZIF-8 and (b) ZIF-8@ZnFc-MOF-M.



**Figure S8** Thermogravimetric analysis of ZIF-8@ZnFc-MOF-M and ZIF-8.

**Figure S9** LSVs of Fe₃C@CNTs/NC-M calcined at 800 ℃ , 920 ℃ and 1000 ℃ in $O_2$ saturated 0.1 M KOH, at 5 mV/s scan rate and 1600 rpm.



**Figure S10** SEM of ZIF-8, Fe₃C@FeN/C-M and Fe₃C@CNTs/NC-M.



**Figure S11** SEM of N/C.
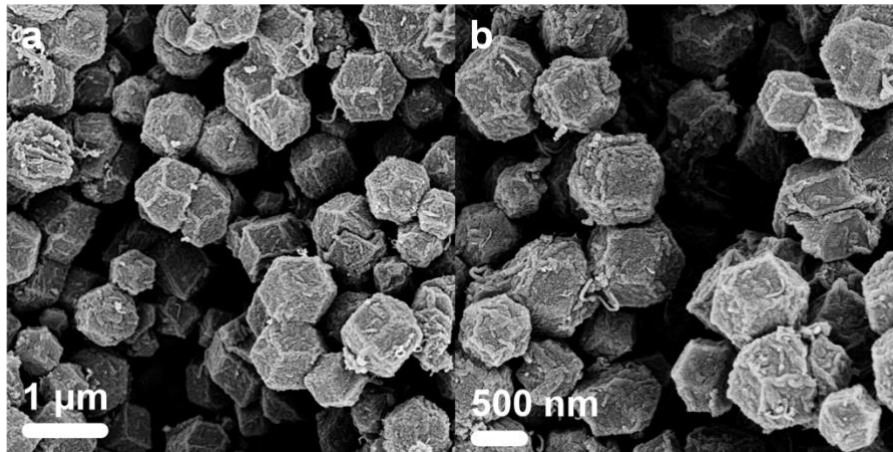
**Figure S12** SEM of Fe$_3$C@CNTs/NC-L.
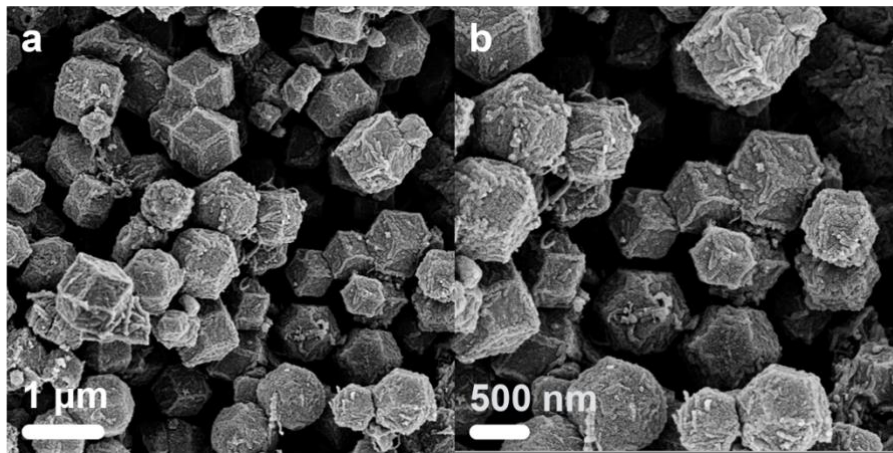

**Figure S13** SEM of Fe$_3$C@CNTs/NC-M.
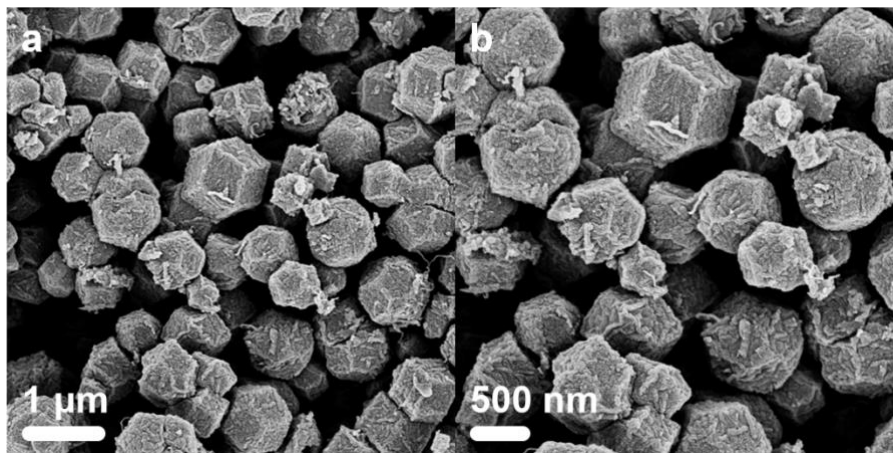

**Figure S14** SEM of Fe$_3$C@CNTs/NC-H.
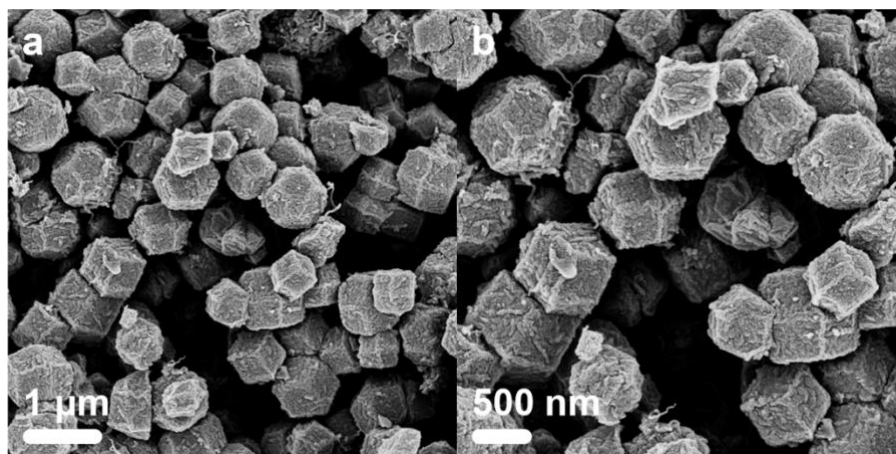
**Figure S15** SEM of Fe₃C@CNTs/NC-Mix.
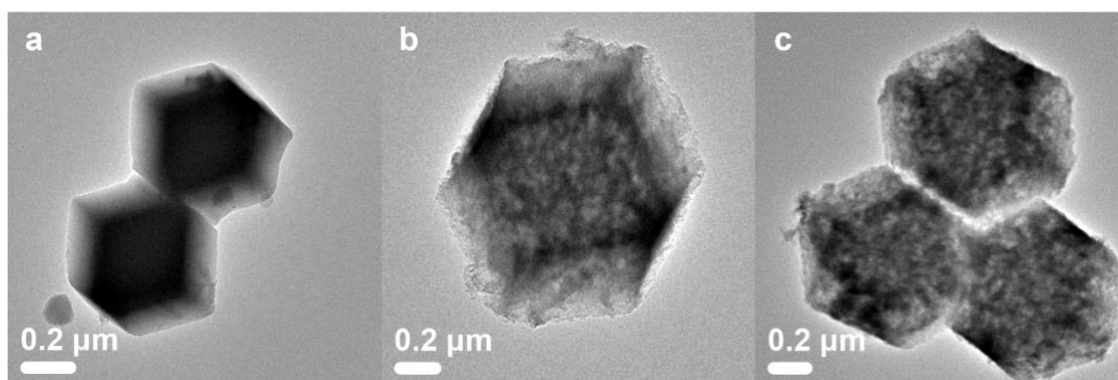


**Figure S16** Bright field TEM of ZIF-8, Fe₃C@FeN/C-M and Fe₃C@CNTs/NC-M (left to right)
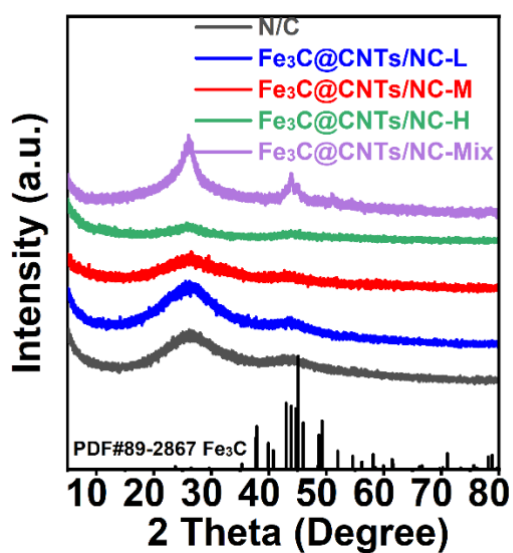


**Figure S17** XRD spectra of N/C and Fe₃C@CNTs/NC-x.
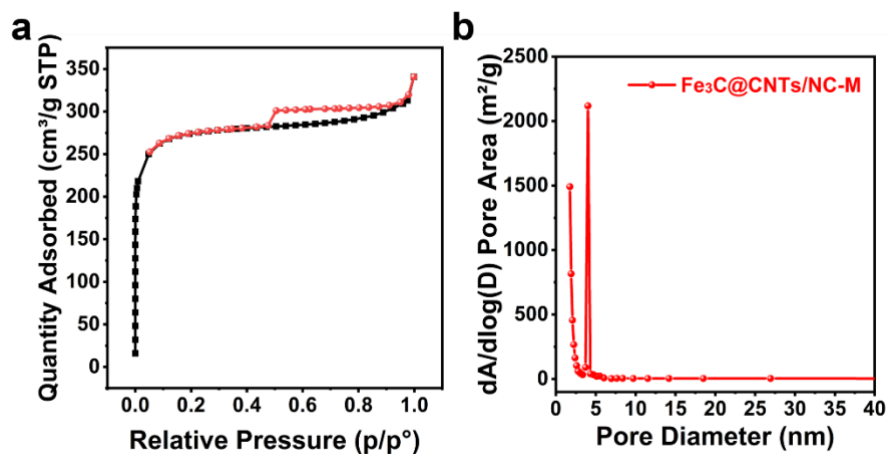
**Figure S18** (a) $N_2$ adsorption–desorption isotherms and (b) corresponding pore size distribution of Fe₃C@CNTs/NC-M.
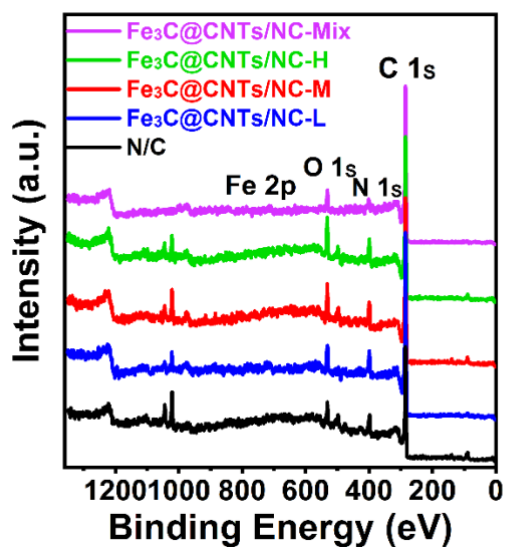


**Figure S19** XPS survey spectra of the various catalysts.
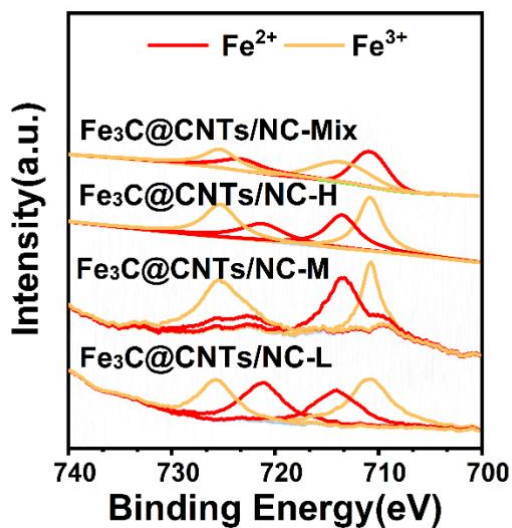
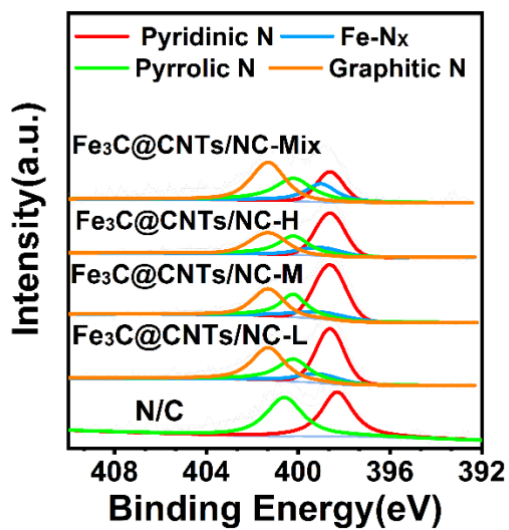**Figure S20** XPS Fe 2p region of Fe₃C@CNTs/NC-x.
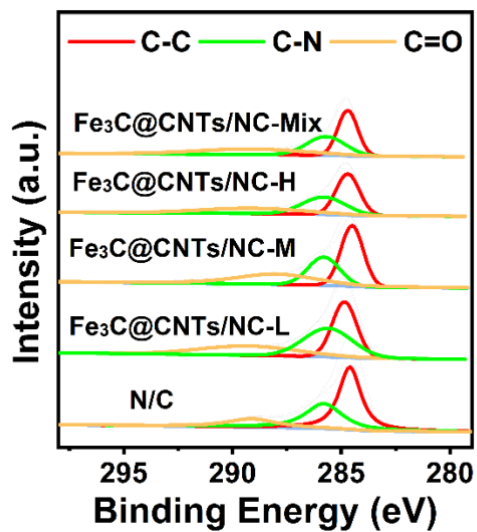


**Figure S21** XPS C 1s region of Fe₃C@CNTs/NC-x.
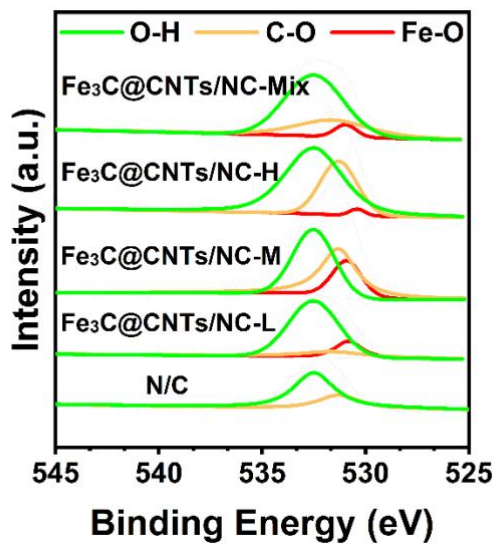
**Figure S22** XPS N 1s region of Fe₃C@CNTs/NC-x.



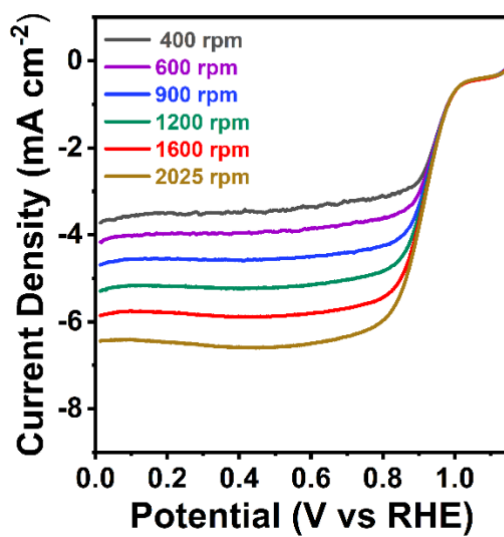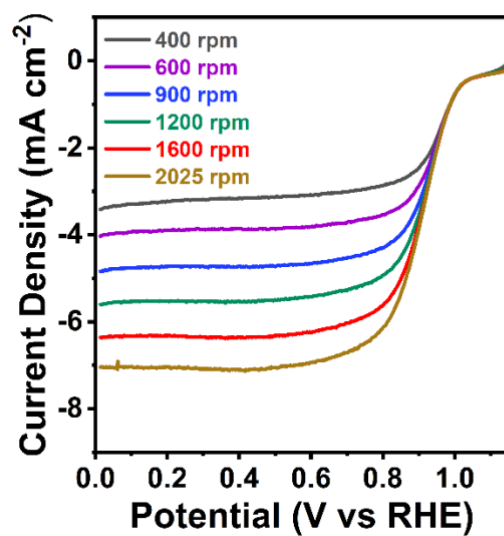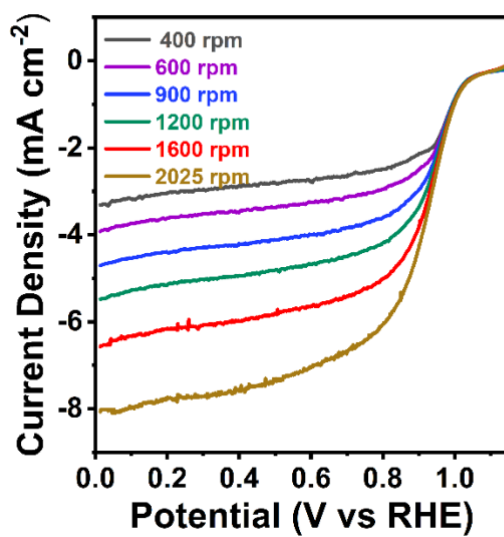**Figure S23** XPS O 1s region of Fe₃C@CNTs/NC-x.
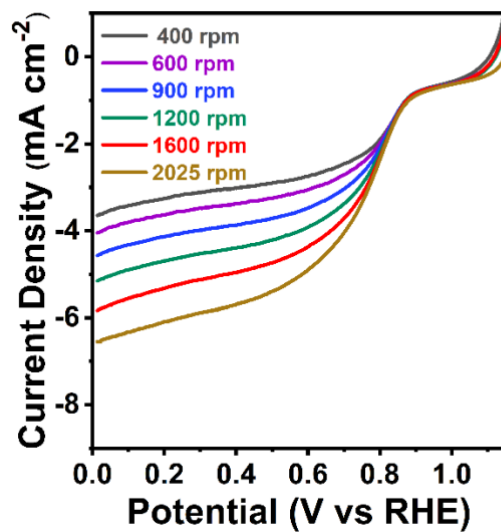
**Figure S24** LSVs of N/C in $O_2$ saturated 0.1 M KOH at different rotation rates.



**Figure S25** LSVs of $Fe_3C$@CNTs/NC-L in $O_2$ saturated 0.1 M KOH at different rotation rates.

**Figure S26** LSVs of Fe$_3$C@CNTs/NC-H in O$_2$ saturated 0.1 M KOH at different rotation rates.



**Figure S27** LSVs of Fe$_3$C@CNTs/NC-Mix in O$_2$ saturated 0.1 M KOH at different rotation rates.
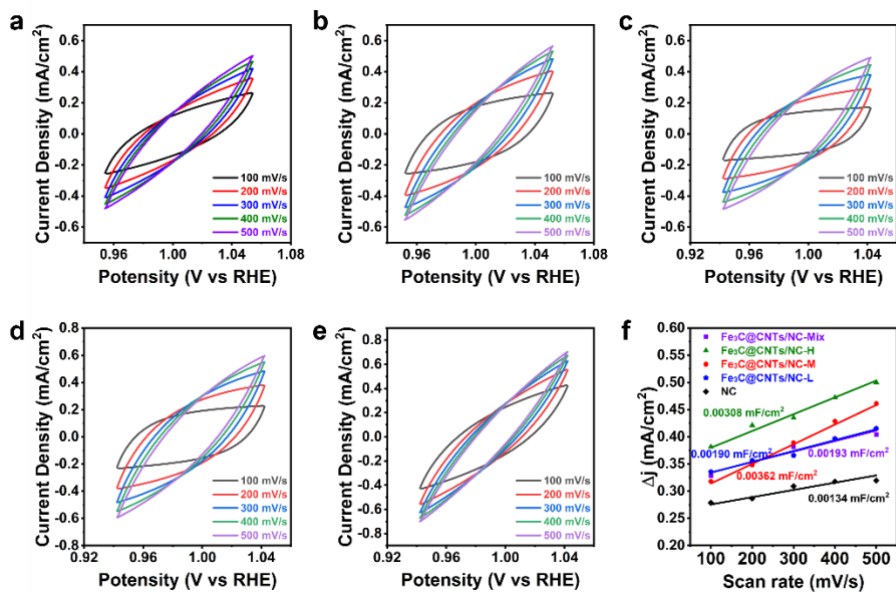
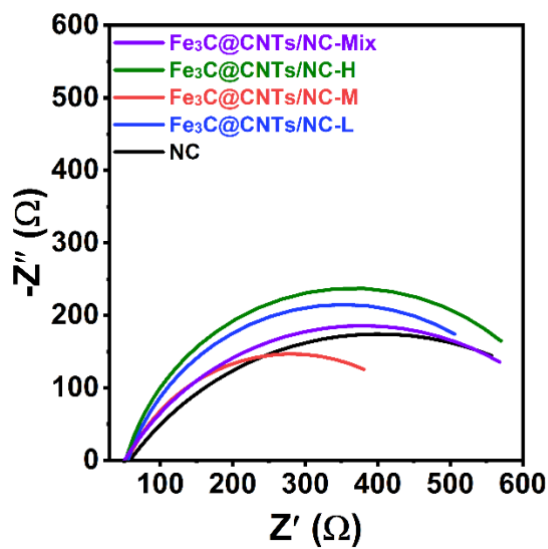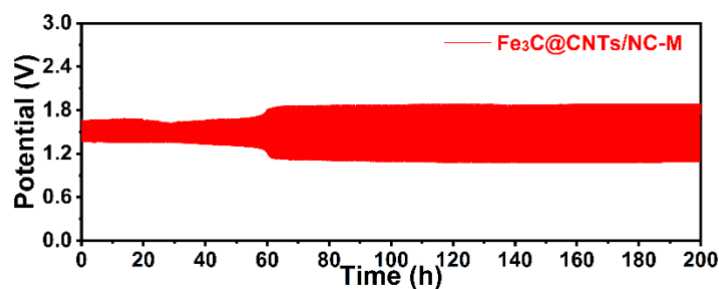**Figure S28** Cdl measurements of N/C and Fe₃C@CNTs/NC-x.



**Figure S29** EIS spectra of N/C and Fe₃C@CNTs/NC-x.

**Figure S30** Photograph of the zinc-air button cell components.



**Figure S31** Charge-discharge cycles of generated and commercial catalysts air electrodes in the zinc-air battery at 1 mA/cm$^2$.

**Table S1** ICP-OES results for Fe content in Fe$_3$C@CNTs/NC-x

| Sample name | Measured element | Quality score |
|---|---|---|
| Fe$_3$C@CNTs/NC-L | Fe | 0.25 % |
| Fe$_3$C@CNTs/NC-M | Fe | 1.46 % |
| Fe$_3$C@CNTs/NC-H | Fe | 2.19 % |

**Table S2** Comparison of ORR properties of Fe$_3$C@CNTs/NC-M and Pt/C with recently reported carbon-based catalysts in 0.1M KOH electrolyte solutions.

| Catalysts | Eonset (V) | E$_{1/2}$ (V) | J$_k$ (mA/cm$^2$) | Ref. |
|---|---|---|---|---|
| Fe$_3$C@CNTs/NC-M | 1.148 | 0.941 | 6.31 | This work |
| Pt/C | 0.918 | 0.746 | 5.30 | This work |
| Co@NCNTs | 0.890 | 0.810 | 7.40 | [22] |
| Fe$_3$C/N,S-CNS | 0.980 | 0.860 | 5.80 | [37] |
| CoZn-NCNTs | 0.940 | 0.820 | 4.50 | [30] |
| FeCo-HNC/CNT | 1.060 | 0.902 | 5.41 | [38] |

| | | | | |
|---|---|---|---|---|
| Fe/12Zn-NCNTs | 0.997 | 0.864 | 4.48 | 33 |
| FeS/Fe$_3$C@NS-C-900 | 1.030 | 0.780 | 4.48 | 42 |
| Fe-N/C-155 | / | 0.850 | 6.00 | 46 |
| Fe$_3$C@C-Fe SAS | 0.990 | 0.910 | / | 47 |
| Fe-NC(Zn$^{2+}$) | / | 0.950 | 5.80 | 48 |
| Fe$_3$C-FeNx/NC-7 | 1.060 | 0.930 | 5.65 | 43 |
| Fe$_3$C-FeN/NC-2 | 0.950 | 0.800 | 5.10 | 49 |
| FeNCFs | 0.990 | 0..840 | 5.92 | 50 |
| Fe/Fe$_3$C@FeN-C-900 | 1.050 | 0.880 | 5.80 | 51 |
| Fe$_3$C@NCNTs | ~ 0.920 | 0.840 | 5.80 | 45 |

# 4 References

1.  Xie T, Hu J, Xu Q, Zhou C. Metal-organic framework derived Fe$_3$C nanoparticles coupled single-atomic iron for boosting oxygen reduction reaction. *J Colloid Interface Sci.* 2023;630:688-697.

2.  Zhao X, He X, Chen B, Yin F, Li G. MOFs derived metallic cobalt-zinc oxide@nitrogen-doped carbon/carbon nanotubes as a highly-efficient electrocatalyst for oxygen reduction reaction. *Appl Surf Sci.* 2019;487:1049-1057.

3.  Ruan QD, Feng R, Feng JJ, Gao YJ, Zhang L, Wang AJ. High-Activity Fe$_3$C as pH-Universal Electrocatalyst for Boosting Oxygen Reduction Reaction and Zinc-Air Battery. *Small.* 2023:2300136.

4.  Liu X, Wang L, Zhang G, et al. Zinc assisted epitaxial growth of N-doped CNTs-based zeolitic imidazole frameworks derivative for high efficient oxygen reduction reaction in Zn-air battery. *Chem Eng J.* 2021;414:127569.

5.  Cheng Y, Hu S, Luo G, Gao Z, Zhang X. FeCoN Co-doped Hollow Carbon Nanocage Grafted with Carbon Nanotubes as an Electrocatalyst for Enhanced Oxygen Reduction Reaction. *ACS Appl Energy Mater.* 2023;6:2010-2021.

6.  Xue J, Deng S, Wang R, Li Y. Efficient synergistic effect of trimetallic organic frameworks derived as bifunctional catalysis for the rechargeable zinc-air flow battery. *Carbon.* 2023;205:422-434.

7.  Li YW, Zhang WJ, Li J, et al. Fe-MOF-Derived Efficient ORR/OER Bifunctional Electrocatalyst for Rechargeable Zinc-Air Batteries. *ACS Appl Mater Interfaces.* 2020;12:44710-44719.

8.  Ye G, He Q, Liu S, et al. Cage-confinement of gas-phase ferrocene in zeolitic imidazolate frameworks to synthesize high-loading and atomically dispersed Fe–N codoped carbon for efficient oxygen reduction reaction. *J Mater Chem A* 2019;7:16508-16515.

9.  Wei X, Song S, Wu N, et al. Synergistically enhanced single-atomic site Fe by Fe$_3$C@C for boosted oxygen reduction in neutral electrolyte. *Nano Energy.* 2021;84:105840.

10. Liu Y, He S, Huang B, Kong Z, Guan L. Influence of different Fe doping strategies on modulating active sites and oxygen reduction reaction performance of Fe, N-doped carbonaceous catalysts. *J Energy Chem.* 2022;70:511-520.

11. Zhou F, Yu P, Sun F, Zhang G, Liu X, Wang L. The cooperation of Fe$_3$C nanoparticles with isolated single iron atoms to boost the oxygen reduction reaction for Zn–air batteries. *J Mater Chem A.* 2021;9:6831-6840.

12. Ma Y, Chen D, Zhang D, et al. Fe,N-modulated carbon fibers aerogel as freestanding cathode catalyst for rechargeable Zn–Air battery. *Carbon.* 2022;187:196-206.

13. Pei F, Chen M, Kong F, Huang Y, Cui X. In-situ coupling FeN nanocrystals with Fe/Fe$_3$C nanoparticles to N-doped carbon nanosheets for efficient oxygen electrocatalysis. *Appl Surf Sci.* 2022;587:152922.

14. Xu C, Guo C, Liu J, et al. Accelerating the oxygen adsorption kinetics to regulate the oxygen reduction catalysis via Fe$_3$C nanoparticles coupled with single Fe-N$_4$ sites. *Energy Storage Mater.* 2022;51:149-158.